Palaeogeography, Palaeoclimatology, Palaeoecology 558 (2020) 109961

Contents lists available at ScienceDirect

Palaeogeography, Palaeoclimatology, Palaeoecology

journal homepage: www.elsevier.com/locate/palaeo

Invited Research Papers

Oceanic chemistry recorded by cherts during the early Cambrian Explosion, South China

Hongjie Zhang[a,b], Haifeng Fan[a,b,*], Hanjie Wen[a,b], Xiangkun Zhu[c], Shihong Tian[d]

[a] State Key Laboratory of Ore Deposit Geochemistry, Institute of Geochemistry, Chinese Academy of Sciences, Guiyang 550081, China
[b] University of Chinese Academy of Sciences, Beijing 100049, China
[c] MNR Key Laboratory of Isotope Geology, Institute of Geology, Chinese Academy of Geological Sciences, Beijing 100037, China
[d] State Key Laboratory of Nuclear Resources and Environment, East China University of Technology, Nanchang 330013, China

ARTICLE INFO

Keywords:
Yangtze Block
Si isotopes
Fe isotopes
Ocean oxygenation
OMZ

ABSTRACT

The early Cambrian ocean was marked by significant redox changes, but the detailed redox evolution of seawater and its relationship to biological expansion are not fully understood. Widespread chert successions are present in lower Cambrian deposits on the Yangtze Block, South China, which have great potential to record oceanic chemistry. Here, we analyze rare earth elements (REE) and Si and Fe isotopes along three regional chert sections to constrain the origin of lower Cambrian cherts and the redox conditions of the early Cambrian ocean. The REE patterns and Si isotopes illustrate that lower Cambrian cherts at the Muyang (MY; Yanjiahe Formation) and Zunyi (ZY; Niutitang Formation) locales originated from the replacement of precursor carbonates and black shales, respectively, whereas cherts at Chuanyanping (CYP; Liuchapo Formation) locale originated from direct chemical precipitation from seawater and/or hydrothermal fluids. All cherts, except for several lower CYP cherts with hydrothermal contributions, primarily preserved seawater chemical signals. The Ce/Ce* and Y/Ho ratios indicate that these cherts were deposited near a suboxic/anoxic interface, where seawater may have been ferruginous overall, while more subtle redox changes, namely, ferruginous (less reducing) and ferruginous (more reducing), were identified by Fe isotopes. Based on new data and previous results, we propose that the early Cambrian ocean on the Yangtze Block was characterized by a stratified redox framework. Before ~535 Ma in the Cambrian, oxic seawater occurred only along the inner shelf (MSC section), below which seawater was primarily ferruginous (less reducing). During ~535–526 Ma, oxic seawater gradually expanded to the outer shelf (MY section) and a metastable ferruginous (more reducing) zone dynamically existed at shelf–slope locations. Temporal and spatial comparisons revealed that the water column on the Yangtze Block may have experienced a progressive deepening of the redoxcline during the early Cambrian (~535–526 Ma). The metastable redox zone may have been an analogue of the modern oxygen minimal zone (OMZ), which is associated with biological activity and high productivity. The occurrence and spatial fluctuation of the metastable ferruginous (more reducing) zone may have been associated with the evolution of small shelly fossils from assemblage 1 (SSF1) to assemblage 3 (SSF3) and their spatial expansion from shelf to slope. Therefore, accompanied by oceanic oxygenation, the occurrence and spatial fluctuation of an OMZ-like metastable zone may have regulated the biological diversification and distribution during the early Cambrian (~535–526 Ma).

1. Introduction

The early Cambrian was a critical period for biological diversification known as the Cambrian Explosion, which was marked by the abrupt replacement of late Ediacaran soft-bodied biota with skeletonized large-body metazoans (Knoll and Caroll, 1999; Marshall, 2006; Erwin et al., 2011). As oxygen is essential for skeletonized metazoans to maintain life (Graham et al., 1995; Canfield and Teske, 1996), oceanic oxygenation has been considered the most likely stimulation for biological diversification across the Ediacaran–Cambrian (E–C) boundary (Knoll and Caroll, 1999). However, several studies have found that oceanic oxygen levels did not radically increase and even intermittently decreased during the early Cambrian (Kimura and Watanabe, 2001; Sperling et al., 2015; Wei et al., 2018), which challenges the traditional

* Corresponding author.
E-mail addresses: zhanghongjie@mail.gyig.ac.cn (H. Zhang), fanhaifeng@mail.gyig.ac.cn (H. Fan), wenhanjie@vip.gyig.ac.cn (H. Wen), xiangkun@cags.ac.cn (X. Zhu), s.h.tian@163.com (S. Tian).

https://doi.org/10.1016/j.palaeo.2020.109961
Received 10 June 2019; Received in revised form 7 August 2020; Accepted 7 August 2020
Available online 12 August 2020
0031-0182/

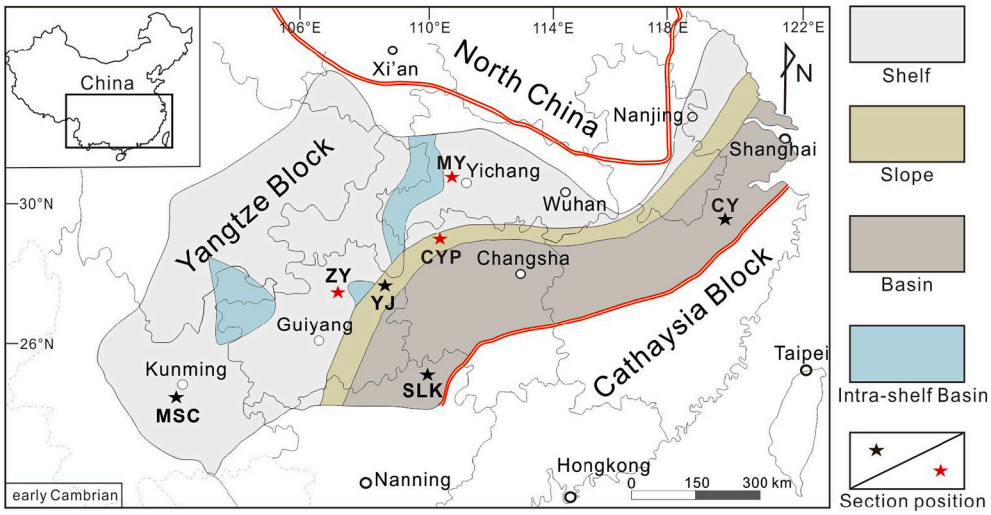

Fig. 1. The paleographic map of South China during the early Cambrian, showing the locations of the studied (red star) and cited (black star) sections in the main text. MSC-Meishucun (Fan et al., 2016), MY-Muyang, ZY-Zunyi, CYP-Chuanyanping, YJ-Yinjiang (Fan et al., 2018), SLK-Silikou (Fan et al., 2018), CY-Chuanye (Xiang et al., 2020).

opinion in which fundamental ocean oxygenation spurred the biological diversification. In contrast, some studies have provided evidence for pronounced oceanic oxygenation during the early Cambrian, although the timing constrained for this oxygenation has been inconsistent. For example, one opinion stated that the remarkable oxygenation in the Nanhua Basin occurred at the beginning of Stage 3 (Wang et al., 2012b; Cai et al., 2015; Chen et al., 2015), while another proposed the start of Stage 4 (Xiang et al., 2017; Li et al., 2017). Following these seemingly different observations, spatially heterogeneous and stratified redox conditions have been suggested for the early Cambrian ocean (Wen et al., 2015; Jin et al., 2016; Guilbaud et al., 2018). In addition, there are differences in the stratified redox framework proposed in previous studies, such as euxinic conditions nested within a ferruginous setting (Feng et al., 2014) or an oxygen minimum zone (OMZ) under an oxic background (Wen et al., 2015; Guilbaud et al., 2018). How did the stratified redox framework evolve, and was the evolution related to biological expansion during the early Cambrian?

The lower Cambrian sedimentary strata are well exposed on the Yangtze Platform in South China, where widespread chert successions continuously or discontinuously overlie the Dengying Formation (Zhu et al., 2003). Previous studies have reported abundant acritarch and metazoan fossils in these cherts (Yang et al., 2016; Ahn and Zhu, 2017; Chang et al., 2017), indicating that these cherts were witnesses to biological evolution in this region. Additionally, recent studies have shown that cherts have broad potential to record the redox conditions in paleo-oceans (Fan et al., 2018; Huang et al., 2018; Xiang et al., 2020) because of their strong chemical stability after consolidation (André et al., 2006; Geilert et al., 2014b). Therefore, these cherts can serve as reliable and effective archives for understanding the linkage between oceanic oxygenation and metazoan diversification on the Yangtze Block. Unfortunately, the origin of regional cherts is poorly understood, despite the efforts of several studies. For example, several studies have shown that regional cherts may have been derived from large-scale hydrothermal activity and/or silica-enriched seawater depending on the location (Wang et al., 2012a; Dong et al., 2015; Gao et al., 2020). These different origins may cause discrepancies in recording oceanic redox signals, especially when the cherts originate from hydrothermal fluids (Chen et al., 2009; Fan et al., 2013). Therefore, understanding the origin of these cherts is a necessary and important first step to interpreting their records of seawater chemistry.

In this study, rare earth elements (REE) and Si and Fe isotopes in three chert sections from the Yangtze Platform were investigated to constrain the origin of the cherts and the oceanic redox conditions during the early Cambrian. The shelf–slope distribution of these three sections and the stratigraphic variation within each section enabled us to identify the spatial and temporal redox evolution of the seawater. By combining with the occurrence and evolution of small shelly fossils, we attempted to determine the relationship between ocean oxygenation and biological explosion on the Yangtze Block during the early Cambrian.

2. Geological setting

2.1. Paleogeography and sedimentary facies

During the early Cambrian, South China was located in the mid-Northern Hemisphere along the northern margin of East Gondwana (Li et al., 2008). South China comprises the Yangtze and Cathaysia blocks, between which the Nanhua Basin was produced during rifting that initiated at ~830–820 Ma (Wang and Li, 2003). Following the cessation of this rifting during the Late Cryogenian, the Nanhua Basin evolved into a passive continental margin along the southeastern side (Jiang et al., 2003). Ediacaran to Cambrian depositional strata are widely distributed on the Yangtze Block, in which the sedimentary facies evolve from northwest to southeast, corresponding with the paleo-water depth gradient (Wang and Li, 2003). Three sedimentary facies were distinguished in previous studies (Steiner et al., 2001; Zhu et al., 2003; Goldberg et al., 2007). The shelf facies mainly consists of carbonates, which are locally interrupted by thin chert deposits (e.g., latest Ediacaran–early Cambrian Yanjiahe Formation). The slope facies is predominantly characterized by black shales (e.g., early Cambrian Niutitang Formation), in which chert deposits are more common than shelf carbonates. The basin facies is primarily characterized by organic-rich black chert with consecutive sequences (e.g., late Ediacaran–early Cambrian Liuchapo Formation). In this study, we investigated three chert sections on the Yangtze Block (Fig. 1) that span from the outer shelf (Muyang-MY in Hubei Province) to the shelf margin (Zunyi-ZY in Guizhou Province) and the slope (Chuanyanping-CYP in Hunan Province). Notably, a local intra-platform basin, in which consecutive shale-chert deposition occurred (fig. 1 in Chang et al., 2019), developed in western Hubei Province during the E–C transition (fig. 1 in Wang et al., 2012a and Dong et al., 2015). The MY section, with thin and intermittent shale-chert bands within predominated carbonates, was close to but not located within the intraplatform basin (Wang et al., 2012a; Dong et al., 2015). Moreover, one inner-shelf section (Meishucun-MSC in Yunnan Province), one slope section (Yinjiang-YJ in Guizhou Province), one basin section (Silikou-SLK in Guangxi Province), and one basin core (Chuanye-CY in Zhejiang Province) were cited for more comprehensive spatial comparisons (Fig. 1).

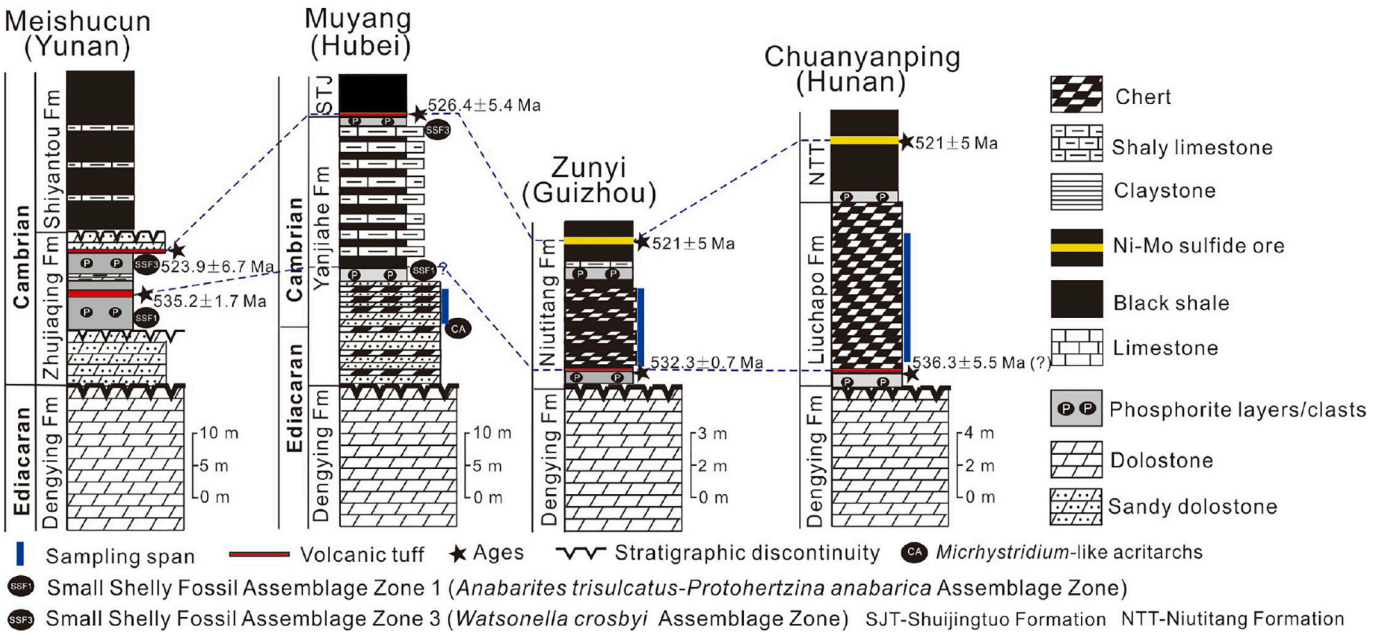

Fig. 2. The stratigraphic columns of the three studied sections on the Yangtze platform and their correlation to the Meishucun section mainly following the chronostratigraphic information and secondarily refering to biostratigraphic information (modified from Jiang et al., 2012). The chronostratigraphic information of the Meishucun (MSC) section was cited from Zhu et al. (2009) and Okada et al. (2014).

2.2. Information about the studied sections

The MY section (30°45′21″N, 111°02′44″E) is located near Muyang village, which is ~20 km from Yichang City, Hubei Province, South China. In this section, the Yanjiahe Formation is overlain by black shales of the Shuijingtuo Formation and underlain by dolostones of the Dengying Formation. The lower Yanjiahe Formation mainly consists of sandy dolostones with interbedded cherts, while the upper Yanjiahe Formation is characterized by limestones with interbedded black shales (Fig. 2). The thickness of the Yanjiahe Formation near Muyang village is ~40 m (Guo et al., 2014) or ~50 m (Ahn and Zhu, 2017; Chang et al., 2019), which largely depends on the definition of the Dengying–Yanjiahe boundary (Chang et al., 2019). For the scenario of ~40-m thickness (adopted here), *Micrhystridium*-like acritarchs were reported to be ~5–15 m above the Yanjiahe–Dengying boundary (Dong et al., 2009; Jiang et al., 2012) and have been suggested to mark the E–C boundary (Ahn and Zhu, 2017; Chang et al., 2019). There are two phosphorite layers in the Yanjiahe Formation: one is located slightly above the horizon of acritarchs and contains small shelly fossils from assemblage 1 (SSF1), and the other is located at the top of the Yanjiahe Formation and contains small shelly fossils from assemblage 3 (SSF3) (Fig. 2; Guo et al., 2014). Moreover, volcanic tuff is present in the basal Shuijingtuo Formation, which was dated to ~526.4 ± 5.4 Ma by using zircon nano-SIMS U–Pb dating (Fig. 2; Okada et al., 2014).

The stratigraphy and petrology of the ZY section (27°41′22″N, 106°40′37″E) were described in detail by Fan et al. (2011) and Pages et al. (2018). In this section, the black shales of the Niutitang Formation are underlain by dolostones of the Dengying Formation (Fig. 2). Here, we focused on only the lowermost ~5 m of the whole Niutitang Formation, where cherts are interbedded with black shales (hereafter, we call this unit the Niutitang Formation exclusively). The boundary between the Dengying and Niutitang formations is characterized by a thin phosphorite layer (~10 cm). Above this phosphorite layer is a K-bentonite layer (tuff), which was dated to 532 ± 0.7 Ma by using zircon SHRIMP U–Pb dating (Jiang et al., 2009). Subsequently, ~3-m cherts that are interbedded with black shales occur, which are overlain by another phosphorite layer. A Ni-Mo sulfide layer (2–15 cm in thickness) is present ~5 m above the basal Niutitang Formation (Pages et al., 2018), for which absolute ages of 521 ± 5 Ma were obtained by Re–Os dating (Xu et al., 2011).

The CYP section (29°11′7″N, 110°54′47″E) is located on the southwestern side of and 10 km from Zhangjiajie City, Hunan Province, South China. At the bottom of this section, the dolostones of the Dengying Formation are present (Fig. 2; Fan et al., 2013). Similarly to the Zunyi section, the Dengying Formation is overlain by a phosphorite layer and volcanic tuff, which are subsequently overlain by a chert unit (consecutive ~10-m sequences). The absolute age of the tuff in this section has not been determined, but this tuff may be correlated to a tuff unit within the Liuchapo Formation in the nearby Ganziping section (~10 km from the CYP section), which was dated to 536.3 ± 5.5 Ma by using zircon SHRIMP U–Pb dating (Chen et al., 2009). Therefore, the ~10-m cherts that overlie the volcanic tuff in this section have been suggested to be part of the Niutitang Formation (Fan et al., 2013). At the top of these cherts, another phosphorite layer is present and is overlain by > 30-m black shales (Niutitang Formation). A Ni-Mo sulfide layer occurs at the base of the black shale sequences, which have identical ages as those in the ZY section (521 ± 5 Ma; Xu et al., 2011) (Fig. 2).

2.3. Regional stratigraphic correlation

In addition to our three studied sections, the MCS section is included in the discussion of the regional stratigraphic correlation (Fig. 2). The MSC section is a former candidate for the Global Stratotype Section and Gold Point for the E–C boundary strata and contains reported Fe-isotope data that are cited later in the discussion (Fan et al., 2016). Here, we predominantly utilized absolute ages to correlate different sections. Based on the available isotope-dating data (Fig. 2), the volcanic tuff in both the basal Niutitang Formation (532.3 ± 0.7 Ma; ZY section) and basal Liuchapo Formation (536.3 ± 5.5 Ma; CYP section) can be correlated to the tuff in the middle Zhujiaqing Formation (535.2 ± 1.7 Ma; MSC section; Zhu et al., 2009). No absolute ages are available for the lower MY section, but biostratigraphic proxies can be used as references. According to recent studies (Ahn and Zhu, 2017; Chang et al., 2019), the E–C boundary may be near the occurrence of *Micrhystridium*-like acritarchs. Therefore, the MY cherts may have been deposited

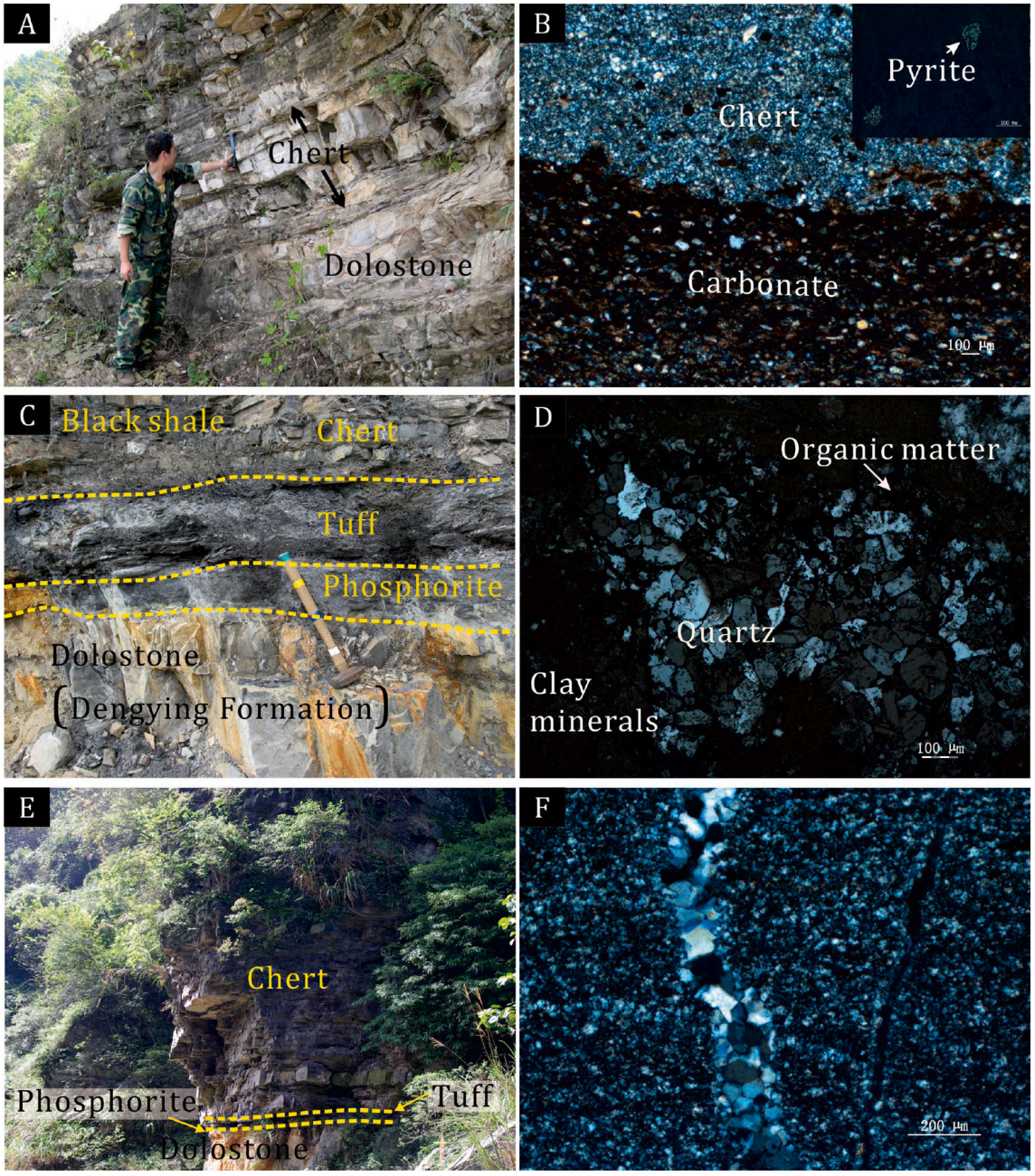

Fig. 3. A. Field photograph of the Muyang (MY) cherts from the lower Yanjiahe Formation, showing that the cherts are interbedded with dolostones. B. Thin section photomicrograph of the representative MY-14 sample, showing major microcrystalline quartz and minor residual carbonate minerals under cross-polarized transmitted light. C. Field photograph of the Zunyi (ZY) cherts from the lower Niutitang Formation, showing that the cherts are interbedded with black shales. D. Thin section photomicrograph of the representative ZY-26 sample, showing major microcrystalline quartz and minor organic matter and clay minerals under cross-polarized transmitted light. E. Field photograph of the Chuanyanping (CYP) cherts from the Liuchapo Formation, showing consecutive chert sequences. F. Thin-section photomicrograph of the representative CYP-08 sample, showing near-pure microcrystalline quartz under cross-polarized transmitted light.

slightly earlier than ~535 Ma and may be slightly older than the ZY and CYP cherts (Fig. 2). The upper correlation can be calibrated by using the ages of the Ni-Mo sulfide layer (521 ± 5 Ma) in the ZY and CYP sections and the absolute ages of the tuff from the upper Zhujiaqing Formation in the MCS section (523.9 ± 6.7 Ma; Okada et al., 2014) and the basal Shuijingtuo Formation in the MY section (526.3 ± 5.4 Ma; Okada et al., 2014) (Fig. 2).

3. Samples and methods

3.1. Samples

Twenty-four fresh cherts and six interbedded rocks (dolostones and black shales) were collected from the three sections described above. In the MY section, cherts commonly occurred as bands with a thickness of a few centimeters within dolostones (Fig. 3A). Six cherts and three interbedded carbonates were collected within an ~4-m span in the lower Yanjiahe Formation. These samples were close to and slightly above the occurrence of *Micrhystridium*-like acritarchs (Fig. 2). Petrography observations showed major microcrystalline and fibrous quartz alongside

Table 1
The rare earth element contents (ppm) and Al contents (%) in cherts and interbedded rocks (dolostones and black shales) of the three studied sections.

Sample	Lithology	La (ppm)	Ce (ppm)	Pr (ppm)	Nd (ppm)	Sm (ppm)	Eu (ppm)	Gd (ppm)	Tb (ppm)	Dy (ppm)	Ho (ppm)
Muyang section											
MY-28	Chert	2.77	5.03	0.85	3.46	0.69	0.16	0.67	0.10	0.43	0.08
MY-29	Chert	3.67	6.53	1.06	4.42	0.93	0.17	0.83	0.12	0.59	0.11
MY-14	Chert	28.30	37.50	6.56	27.40	4.65	1.08	4.57	0.66	3.12	0.62
MY-16	Chert	7.31	12.10	2.27	9.58	1.73	0.37	1.62	0.21	1.05	0.19
MY-18	Chert	5.09	8.36	1.32	5.00	0.91	0.20	0.84	0.14	0.62	0.13
MY-19	Chert	3.73	6.46	0.97	3.85	0.72	0.14	0.81	0.11	0.60	0.13
MY-13	Dolostone	9.56	14.20	2.02	7.96	1.35	0.30	1.26	0.18	1.00	0.23
MY-15	Dolostone	7.34	10.40	1.61	5.84	1.03	0.22	1.06	0.16	0.78	0.17
MY-17	Dolostone	11.10	14.10	2.20	8.41	1.45	0.30	1.33	0.20	1.03	0.21
Zunyi section											
XZ-13	Chert	7.12	8.10	1.79	7.94	1.88	0.43	2.45	0.35	2.16	0.47
XZ-16	Chert	1.29	1.39	0.29	1.31	0.31	-	0.46	0.06	0.41	0.09
XZ -18	Chert	3.39	3.45	0.79	3.49	0.80	0.13	1.11	0.15	1.04	0.24
XZ -20	Chert	3.77	4.39	0.70	2.87	0.63	0.10	0.75	0.12	0.89	0.21
XZ -22	Chert	3.16	3.68	0.77	3.55	0.91	0.19	1.25	0.19	1.34	0.30
XZ -26	Chert	13.33	14.77	2.68	10.82	2.15	0.36	2.67	0.44	3.15	0.74
XZ -28	Chert	3.99	6.33	0.97	3.86	0.90	0.09	1.19	0.23	1.67	0.36
XZ-19	Black shale	60.53	67.67	11.92	47.89	9.84	1.75	11.80	1.89	13.62	3.20
XZ-21	Black shale	37.43	45.11	8.39	35.86	7.69	1.37	9.83	1.52	10.97	2.62
XZ-27	Black shale	61.94	76.20	12.21	48.20	10.48	1.38	14.44	2.70	20.90	5.04
Chuanyanping section											
CYP-11	Chert	1.97	2.47	0.31	1.03	0.18	0.11	0.21	0.04	0.30	0.09
CYP-10	Chert	2.20	2.74	0.71	0.97	0.13	0.08	0.21	0.03	0.26	0.08
CYP-09	Chert	2.15	2.89	0.35	1.15	0.18	0.29	0.19	0.04	0.28	0.08
CYP-8.5	Chert	2.47	2.80	0.34	1.02	0.18	0.10	0.22	0.05	0.36	0.09
CYP-08	Chert	0.46	0.65	0.08	0.22	0.08	0.04	0.08	0.02	0.13	0.03
CYP-07	Chert	2.99	3.77	0.52	1.60	0.19	0.89	0.35	0.04	0.30	0.08
CYP-06	Chert	2.16	2.66	0.32	0.98	0.19	0.41	0.18	0.04	0.26	0.07
CYP-05	Chert	1.53	2.08	0.28	0.84	0.17	0.48	0.19	0.03	0.26	0.07
CYP-04	Chert	4.81	5.53	0.81	2.00	0.26	1.64	0.37	0.05	0.30	0.10
CYP-03	Chert	5.89	7.69	1.09	3.25	0.33	0.78	0.40	0.07	0.47	0.13
CYP-02	Chert	7.89	9.68	1.22	3.61	0.51	1.10	0.47	0.10	0.76	0.22

Sample	Er (ppm)	Tm (ppm)	Yb (ppm)	Lu (ppm)	Y (ppm)	ΣREE (ppm)	Ce/Ce*	Pr/Pr*	Eu/Eu*	Y/Ho	Al (%)
Muyang section											
MY-28	0.18	0.02	0.12	0.02	2.54	17.12	0.75	1.17	1.18	31.75	0.88
MY-29	0.25	0.04	0.23	0.03	3.57	22.55	0.76	1.13	0.96	32.45	0.39
MY-14	1.33	0.12	0.51	0.06	23.10	139.58	0.64	1.16	1.19	37.26	0.25
MY-16	0.37	0.04	0.22	0.04	5.68	42.78	0.68	1.18	1.15	29.89	0.60
MY-18	0.36	0.05	0.30	0.04	4.04	27.40	0.74	1.18	1.09	31.08	0.64
MY-19	0.28	0.04	0.26	0.03	3.97	22.10	0.78	1.13	0.97	30.54	0.55
MY-13	0.58	0.08	0.53	0.07	6.50	45.82	0.74	1.11	1.16	28.26	1.63
MY-15	0.44	0.06	0.36	0.05	4.91	34.43	0.70	1.20	1.06	28.88	0.95
MY-17	0.59	0.08	0.47	0.07	6.28	47.82	0.66	1.17	1.07	29.90	1.44
Zunyi section											
XZ-13	1.37	0.18	1.12	0.15	19.34	54.85	0.52	1.21	1.06	41.15	1.54
XZ-16	0.30	0.04	0.29	0.05	3.58	9.87	0.52	1.17	-	39.78	0.27
XZ -18	0.73	0.10	0.60	0.08	11.01	27.11	0.49	1.22	0.75	45.88	0.80
XZ -20	0.68	0.11	0.75	0.11	7.20	23.28	0.62	1.13	0.73	34.29	2.90
XZ -22	0.96	0.14	0.88	0.13	13.06	30.51	0.54	1.16	0.92	43.53	3.58

(*continued on next page*)

Table 1 (*continued*)

Sample	Er (ppm)	Tm (ppm)	Yb (ppm)	Lu (ppm)	Y (ppm)	ΣREE (ppm)	Ce/Ce*	Pr/Pr*	Eu/Eu*	Y/Ho	Al (%)
XZ -26	2.30	0.33	2.13	0.31	28.87	85.05	0.57	1.20	0.75	39.01	3.03
XZ -28	1.05	0.15	0.95	0.14	12.09	33.97	0.74	1.14	0.40	33.58	1.40
XZ-19	10.11	1.40	8.80	1.27	143.80	395.49	0.58	1.19	0.81	44.94	4.77
XZ-21	8.38	1.21	7.84	1.17	116.80	296.19	0.59	1.17	0.80	44.58	4.27
XZ-27	15.93	2.37	15.42	2.29	202.60	492.10	0.64	1.16	0.53	40.20	2.06
Chuanyanping section											
CYP-11	0.29	0.05	0.34	0.05	2.66	10.10	0.72	1.14	2.63	29.56	0.68
CYP-10	0.25	0.04	0.29	0.05	2.09	10.13	0.50	2.55	2.60	26.13	0.54
CYP-09	0.26	0.04	0.29	0.05	2.30	10.54	0.76	1.13	6.92	28.75	0.61
CYP-8.5	0.30	0.05	0.37	0.05	2.85	11.25	0.68	1.18	2.15	31.67	0.63
CYP-08	0.11	0.02	0.15	0.03	1.04	3.14	0.77	1.24	2.04	34.67	0.24
CYP-07	0.27	0.05	0.32	0.06	2.33	13.76	0.69	1.25	20.61	29.13	0.76
CYP-06	0.23	0.04	0.26	0.04	2.01	9.85	0.72	1.16	9.49	28.71	0.54
CYP-05	0.21	0.04	0.26	0.04	1.79	8.27	0.73	1.25	13.34	25.57	0.47
CYP-04	0.34	0.05	0.38	0.07	2.51	19.22	0.64	1.43	28.81	25.10	0.77
CYP-03	0.48	0.09	0.61	0.10	3.78	25.16	0.70	1.28	10.36	29.08	1.08
CYP-02	0.65	0.11	0.87	0.13	5.55	32.87	0.71	1.21	9.77	25.23	2.07

The REE data of the CYP cherts were cited from Fan et al. (2013), except one new data (CYP-8.5). ΣREE are the sum of all rare earth elements and Y contents, $Ce/Ce^* = Ce_N/(0.5La_N + 0.5Pr_N)$, $Pr/Pr^* = Pr_N/(0.5Ce_N + 0.5Nd_N)$, $Eu/Eu^* = Eu_N/(0.67Sm_N + 0.33Tb_N)$. "-" mean abnormal values.

minor carbonate residuals and diagenetic pyrites (~100 μm) in these cherts (Fig. 3B). In the ZY section, the cherts were interbedded with black shales (Fig. 3C). Seven cherts and three interbedded black shales were sampled within an ~3-m span in the Niutitang Formation. In addition to the major microcrystalline quartz, some organic matter and clay minerals were observed in the ZY cherts (Fig. 3D). In the CYP section, the cherts occurred as thick continuous bands (Fig. 3E). Eleven cherts were sampled within an ~7-m span in the Liuchapo Formation. Microphotography showed nearly pure microcrystalline and fibrous quartz in the CYP cherts, locally with quartz veins crossing the sedimentary sequence (Fig. 3F).

3.2. Methods

3.2.1. Major- and trace-element concentrations

The samples were crushed into 200-mesh powder, and then ~4-g powder samples were mixed with 7 g of lithium tetraborate powder in a platinum crucible. The mixture was melted and pelleted into fused glass at a high temperature of > 1000 °C for 2 h. The major elements were determined by X-ray fluorescence (XRF) at ALS Chemex Co., Ltd. (Guangzhou). Standard reference materials were analyzed together with unknown samples, and the precision was better than 5% (Fan et al., 2013).

Powder samples (~50 mg) were digested in Savillex vials by using ultra-pure HF and HNO_3 at high temperature (T > 140 °C) for 72 h. After complete digestion and HF-HNO_3 evaporation, the samples were diluted in 3% HNO_3 with a quantitative Rh internal standard solution. The clear solution was analyzed for trace elements and REE by using inductively coupled plasma mass spectrometry (ICP-MS) at the Institute of Geochemistry, Chinese Academy of Sciences (CAS). The precision was better than 3%, as determined from the results of the standard reference materials of GBPG-1 (garnet-biotite plagiogneiss), OU-6 (Penrhyn slate), and AMH-1 (Mount Hood andesite) (Qi et al., 2000).

3.2.2. Silicon isotopes

The measurement of Si isotopes followed the procedure reported by Ding (2004). Powder samples (~100 mg) were batched with concentrated HCl at 80 °C for 12 h to remove carbonates and sulfides. The solution was filtered, and the residue was washed at least in triplicate with Milli-Q water. The residue was then dried at 100 °C in an oven and ashed at 500 °C in a muffle furnace to remove organic material. After these pretreatments, SiO_2 was converted to SiF_4 through reaction with BrF_5 in a metal vacuum system (Clayton and Mayeda, 1963). SiF_4 was first separated from O_2, N_2, BrF_3, and BrF_5 through several stages of distillation and condensation at liquid-nitrogen temperatures. Subsequently, SiF_4 was purified from other active fluorine compounds by transfer through a Cu tube that contained pure Zn particles at 60 °C. The Si-isotope ratios were then analyzed with a MAT-253 gas-source isotope ratio mass spectrometer at the Institute of Mineral Resources, CAGS. The accuracy and reproducibility of the analyses were evaluated through repeated measurements of two Chinese national reference materials, namely, GBW04421 ($\delta^{30}Si$ = 0.0‰) and GBW04422 ($\delta^{30}Si$ = -2.6‰), which yielded a total analytical precision of better than ± 0.1‰. All the Si-isotope compositions are reported relative to the NBS-28 reference material.

3.2.3. Iron isotopes

Powder samples (~200 mg) were ashed at 500 °C to degrade organic material and then digested by using an acid mixture of ultra-pure HF and HNO_3 at 120 °C for 24 h. After the complete digestion and evaporation of HF and HNO_3, the samples were diluted in 6N HCl acid. The chemical purification for Fe-isotope analysis was conducted with AGMP-1 resin following the methods of Tang et al. (2006). The Fe-isotope compositions were measured by using a Nu multi-collector ICP-MS at the Institute of Geology, CAGS. The Fe-isotope compositions were expressed in standard notation as the $\delta^{56}Fe$ deviation from IRMM-014.

Table 2
The $\delta^{30}Si$ and $\delta^{56}Fe$ values, and major and trace elements in cherts from the three studied sections.

Sample	Lithology	$\delta^{30}Si$ (‰)	$\delta^{57}Fe$ (‰)	2σ (‰)	$\delta^{56}Fe$ (‰)	2σ (‰)	SiO_2 (%)	Fe (%)	V (ppm)	Ni (ppm)	Ba (ppm)	Fe/Al
Muyang section												
MY-28	Chert	0.8	0.61	0.12	0.42	0.12	93.23	0.32	9	5	173	0.36
MY-29	Chert	0.7	0.82	0.04	0.56	0.08	95.26	0.12	35	10	206	0.31
MY-14	Chert	-0.3	0.65	0.13	0.41	0.10	93.88	0.20	17	5	171	0.80
MY-16	Chert	0.6	0.57	0.13	0.39	0.13	94.00	0.29	15	6	252	0.48
MY-18	Chert	0.9	0.60	0.05	0.44	0.03	87.69	0.36	16	6	177	0.56
MY-19	Chert	0.5	0.67	0.16	0.47	0.11	91.88	0.29	14	15	506	0.53
Zunyi section												
XZ-13	Chert	0.0	0.63	0.17	0.43	0.12	80.87	1.25	323	82	894	0.81
XZ-16	Chert	-0.2	0.76	0.03	0.56	0.02	91.62	0.42	219	34	2350	1.56
XZ -18	Chert	-0.1	0.78	0.01	0.54	0.06	89.29	0.43	193	44	2125	0.54
XZ -20	Chert	-0.1	1.40	0.06	0.98	0.04	83.06	0.67	639	88	746	0.23
XZ -22	Chert	-0.1	1.19	0.08	0.82	0.04	79.44	1.31	470	54	954	0.37
XZ -26	Chert	-0.2	1.09	0.00	0.74	0.08	80.43	0.71	2064	81	837	0.23
XZ -28	Chert	-0.2	1.42	0.01	0.99	0.04	91.66	0.70	776	33	408	0.50
Chuanyanping section												
CYP-11	Chert	1.1	1.42	0.03	0.98	0.03	95.89	0.26	12	7	464	0.38
CYP-10	Chert	1.0	1.20	0.02	0.82	0.01	95.76	0.17	11	8	366	0.31
CYP-09	Chert	1.2	0.68	0.10	0.46	0.00	96.50	0.29	11	5	1690	0.48
CYP-8.5	Chert	-	0.53	0.01	0.35	0.14	95.84	0.27	20	7	501	0.43
CYP-08	Chert	0.4	0.59	0.09	0.43	0.09	97.10	0.08	15	8	206	0.34
CYP-07	Chert	0.7	0.58	0.09	0.41	0.05	94.99	0.14	53	3	5750	0.18
CYP-06	Chert	0.5	0.39	0.04	0.32	0.03	95.02	0.46	25	4	2400	0.85
CYP-05	Chert	0.2	0.42	0.02	0.26	0.02	96.28	0.09	19	7	2750	0.19
CYP-04	Chert	0.1	0.32	0.00	0.24	0.00	93.07	0.18	28	5	9950	0.24
CYP-03	Chert	-0.3	-0.64	0.05	-0.41	0.05	90.92	0.77	53	7	4480	0.71
CYP-02	Chert	-0.5	0.07	0.05	0.06	0.00	85.00	0.45	73	7	6830	0.22

The SiO_2, Fe, and Ni contents of the ZY cherts were cited from Fan et al. (2011), except the XZ-22. The SiO_2, Al, V, Ni and Ba contents, and $\delta^{30}Si$ values of the CYP cherts were cited from Fan et al. (2013), except the CYP-8.5. "-" mean not measured.

The accuracy and long-term reproducibility of each analytical run were tested by routine analyses of a laboratory standard (GSR-3, $\delta^{56}Fe$ = 0.23‰) and an international geostandard (BHVO-1, $\delta^{56}Fe$ = 0.11‰), and the long-term external reproducibility (2σ) of the $\delta^{56}Fe$ measurements following this method was ± 0.10‰ (Zhao et al., 2012).

4. Results

4.1. Major and trace elements

The results of major and trace elements are shown in Tables 1 and 2. The MY and CYP cherts were characterized by relatively constant and high concentrations of SiO_2, mostly exceeding 93.00%. These cherts contained low Al (mostly between 0.24% and 1.08%) and Fe (mostly between 0.08% and 0.46%) concentrations. In contrast, the ZY cherts yielded lower and more variable concentrations of SiO_2 (79.44% to 91.66%) but higher Al (mostly between 0.80% and 3.58%) and Fe (0.43%–1.30%) concentrations.

Shale (post-Archean Australian shale, PAAS)-normalized REE patterns are shown in Fig. 4. The REE patterns of the MY cherts were characterized by apparent negative Ce anomalies (0.64–0.78), negligible Eu anomalies (0.96–1.19), and superchondritic Y/Ho ratios (average value of 32). The ZY cherts showed negative Ce (0.49–0.74) and Eu anomalies (0.40–1.06) and superchondritic Y/Ho ratios (average value of 39). Relatively high concentrations of total REE (ΣREE) were observed in the ZY cherts, mostly ranging from 23.28 to 85.05 ppm, which may reflect contributions from continental clay minerals (Fig. 3D). The CYP cherts exhibited obvious positive Eu anomalies (2.04–27.28.81), which may have resulted from hydrothermal activities (Fan et al., 2013). Additionally, these cherts had more variable and lower Y/Ho ratios (25.10 to 34.67) than those in the other two sections.

4.2. Silicon isotopes of whole rocks

The Si-isotope results are shown in Table 2. The three groups of cherts in this study showed different characteristics of Si-isotope composition. The $\delta^{30}Si$ values of the MY cherts clustered within a narrow range from 0.5‰ to 0.9‰ (except for one value, -0.3‰), with an average value of 0.7‰. The ZY cherts were characterized by identical ~0.0‰ and slightly negative $\delta^{30}Si$ values from -0.2‰ to 0.0‰. In contrast to the ZY and MY cherts, the CYP cherts possessed widely varying $\delta^{30}Si$ values from -0.5‰ to 1.2‰ (Fan et al., 2013). There was an increasing trend in $\delta^{30}Si$ values from the bottom to the top of the Lliuchapo Formation in this section.

4.3. Iron isotopes of whole rocks

The Fe-isotope results are reported in Table 2. The $\delta^{56}Fe$ values ranged from -0.41‰ in the CYP cherts to 0.99‰ in the ZY cherts but were mostly positive. The $\delta^{56}Fe$ values of the MY cherts were relatively constant, with an average of 0.45‰. In contrast, the ZY and CYP cherts were characterized by a bimodal distribution of lower $\delta^{56}Fe$ values (mostly between 0.20‰ and 0.50‰) and higher $\delta^{56}Fe$ values (0.74‰ to 0.99‰). Interestingly, the ZY cherts showed decreasing $\delta^{56}Fe$ values from the bottom to the top, whereas the $\delta^{56}Fe$ values in the CYP cherts increased systematically.

5. Discussion

5.1. Origin mechanisms of cherts

Marine sedimentary cherts generally have three fundamental origin mechanisms: diagenetic replacement of precursor sediments, direct chemical precipitation from seawater, and hydrothermal activity (Van den Boorn et al., 2010; Fan et al., 2013; Dong et al., 2015; Brengman and Fedo, 2018; Shen et al., 2018). According to previous studies, the

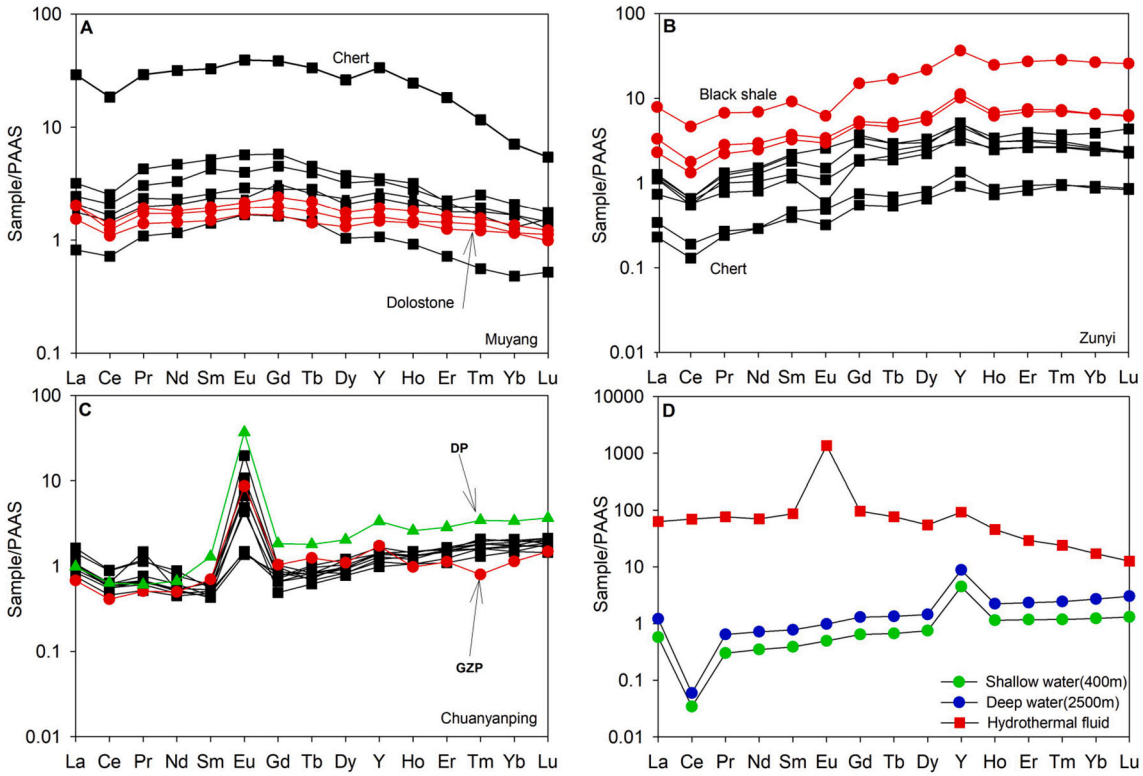

Fig. 4. PAAS-normalized REE + Y patterns of cherts and several interbedded rocks (dolostones and black shales) in the three studied sections compared with those of modern oxic seawater (Alibo and Nozaki, 1999) and high-temperature hydrothermal fluids (Bau et al., 1996). The data for the Ganzipin (GZP) and Dapin (DP) cherts were cited from Wang et al. (2012a). The dolostones of MY-13, MY-15, and MY-17 are located around the cherts of MY-14 and MY-16, respectively, the black shales of ZY-19, ZY-21, and ZY-27 are located around the cherts of ZY-20 and ZY-26, respectively.

E–C transition cherts on the Yangtze Block may have different origin mechanisms. For example, Dong et al. (2015) and Gao et al. (2020) found that cherts at the SLK locale and Upper–Middle Yangtze area originated from either diagenetic alteration of precursor sediments or direct deposition from seawater. In contrast, Chen et al. (2009) and Wang et al. (2012a) proposed that cherts in western Hunan Province mostly originated from hydrothermal fluids. The MY and ZY cherts were interbedded with dolostones and black shales, respectively (Fig. 3A and C), and retained their residues (Fig. 3B and D), which may indicate that these cherts were formed by the replacement of precursor sediments. In contrast, the CYP cherts were consecutive sequences and dearth of precursor ghosts based on the stratigraphic context and petrographic observations (Fig. 3E and F). Thus, the CYP cherts may have been derived from direct chemical precipitation from seawater and/or hydrothermal fluids. The stratigraphic background and petrographic observations provide a skeleton for the origin mechanisms of the studied cherts, and additional details can be determined from the geochemical characteristics of these cherts (Brengman and Fedo, 2018; Shen et al., 2018).

5.1.1. *Indications from rare earth elements*

In the MY cherts (Fig. 4A), the REE patterns showed negative Ce anomalies, obscure Eu anomalies, and superchondritic Y/Ho ratios (average value of 32), which are comparable to the REE characteristics of modern seawater (Alibo and Nozaki, 1999). However, the MY cherts also exhibited heavy-REE (HREE) depletion, which contrasts with modern seawater (Fig. 4D). Detrital contamination may affect the chemically deposited REE signals of cherts (Wen et al., 2016), but this speculation can be discounted based on the lack of correlations between the ΣREE and Al concentrations (Fig. 5A). Marine sedimentary carbonates are often depleted in HREE, owing to the decreasing partition coefficients of REE between carbonate and seawater with increasing REE atomic number (Zhong and Mucci, 1995). The MY carbonates also presented depletion in HREE, similarly to the regional carbonates that were reported by Ling et al. (2013) and Wen et al. (2016), who argued that these carbonates primarily recorded REE signals of seawater. The MY section (Fig. 4A) had identical REE patterns in the cherts and interbedded dolostones, indicating that the MY cherts may have inherited the REE signatures of precursor dolostones during diagenetic replacement. This observation is coincident with the reports by Van den Boorn et al. (2010), who proposed that the REE signals of carbonates can (partially) survive diagenetic alteration. Therefore, we argue that the MY cherts predominantly recorded the REE signatures of seawater through diagenetic replacement, despite the depletion in HREE because of parental carbonate discrimination (Zhong and Mucci, 1995).

Except for markedly negative Eu anomalies (Fig. 4B), the ZY cherts showed modern seawater-like REE patterns with HREE enrichment, negative Ce anomalies, and superchondritic Y/Ho ratios (average value of 39). As indicated by the relatively high ΣREE and Al concentrations and their positive correlation (Fig. 5A), the REE signatures of the ZY cherts may have been affected by silicate detritus (Ling et al., 2013; Wen et al., 2016). Indeed, the Zunyi cherts have REE patterns identical to those of paragenetic shales, suggesting REE retention during diagenetic replacement, similarly to the MY cherts. Generally, PAAS shale-normalized REE patterns of silicate detritus should be flat (Nothdurft et al., 2004), while the interbedded black shales (silicate detritus) in the ZY section yielded seawater-like REE patterns, except for the negative Eu anomalies. Brengman and Fedo (2018) observed that seawater-rock interactions during the silicification of volcanics gradually produce silicified rocks with seawater-like REE signals. Thus, the seawater-like REE signatures in the ZY shales may be attributed to extensive seawater-rock interactions during silicification (Rouchon and Orberger, 2008; Rouchon et al., 2009). Additionally, negative Eu anomalies are common in mafic volcanics because of their low plagioclase content

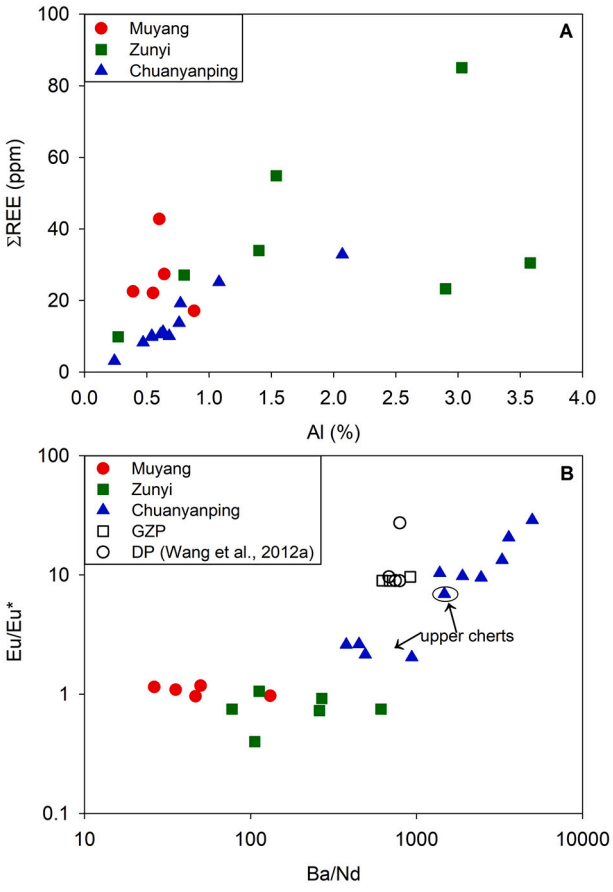

Fig. 5. A. The comparison between total the rare earth elements (ΣREE) and Al contents of the studied cherts (not showing the abnormal MY-14), reflecting the ΣREE in the Zunyi (ZY) cherts may have detrital contributions. B. The correlation between Eu/Eu* and Ba/Nd ratios of the studied cherts, indicating that partial Eu/Eu* of the Chuanyanping (CYP) cherts may be artificial.

(Basu et al., 1991), which may explain the negative Eu anomalies in the ZY shales. It is possible that the ZY shales possessed less plagioclase enrichment than the PAAS shales, and thus, negative Eu anomalies occurred in the ZY shales. Therefore, we maintain that the ZY cherts predominantly documented the REE signals of seawater through diagenetic replacement, despite the negative Eu anomalies.

The REE patterns of the CYP cherts were previously discussed by Fan et al. (2013). The CYP cherts were marked by pronounced positive Eu anomalies (Fig. 4C), similarly to the nearby Ganzipin and Dapin sections (Wang et al., 2012a), which may indicate intensive hydrothermal activities (Derry and Jacobsen, 1990). However, positive Eu anomalies might also result from hydrothermal Ba interference during measurement (Dulski, 1994), which can be detected by the correlations between Eu/Eu* and Ba/Nd (Ling et al., 2013). The obvious positive correlations between Eu/Eu* and Ba/Nd suggest that the positive Eu anomalies in the CYP cherts may be artificial (Fig. 5B). Nevertheless, partial positive Eu anomalies may be real because several ZY cherts with similarly high Ba contents did not have correspondingly positive Eu anomalies (Fig. 5B). Moreover, an extremely high Ba content in cherts is a characteristic of hydrothermal products (Urabe and Kusakabe, 1990; Stuben et al., 1994). The Eu anomalies and Ba contents in the CYP cherts showed a bimodal distribution: the six lower cherts yielded higher Eu/Eu* values and Ba contents than the five upper cherts (Fig. 5B), indicating that hydrothermal activity decreased abruptly across the CYP section. The REE patterns of the CYP cherts, except for the positive Eu anomalies, were still comparable to those of seawater. Therefore, we propose that the CYP cherts documented mixed REE signals from seawater and hydrothermal fluids. The six lower cherts were dominated by hydrothermal fluids, whereas the five upper cherts were mainly controlled by seawater.

5.1.2. Indications from silicon isotopes

The three groups of cherts in this study differed in their Si-isotope compositions: the MY cherts showed positive and relatively homogeneous $\delta^{30}Si$ values (0.5‰ to 0.9‰, except for one value of -0.3‰), the ZY cherts yielded identical $\delta^{30}Si$ values of ~0‰ (-0.2‰ to 0.0‰), and the CYP cherts possessed widely varying $\delta^{30}Si$ values (-0.5‰ to 1.2‰). Early diagenesis may have redistributed Si isotopes in internal microquartz through their dissolution and reprecipitation in precursor sediments (Marin-Carbonne et al., 2012; Tatzel et al., 2015). However, previous studies have shown that this process would not have significantly modified the Si-isotope signals of the bulk cherts if the transformation from precursor sediments to cherts did not involve external fluids (Heck et al., 2011; Ziegler and Marin-Carbonne, 2012; Li et al., 2014; Tatzel et al., 2015). Additionally, postdiagenetic metamorphism and metasomatism are also supposed to have minor effects on the Si-isotope signals of cherts because of their strong chemical stability and extremely abundant Si (André et al., 2006; Heck et al., 2011; Geilert et al., 2014b). Therefore, the different $\delta^{30}Si$ values of the studied cherts may predominantly reflect the distinct sources and conditions of initial deposition.

The cherts that were derived from the silicification of volcanic rocks (S-cherts) were generally characterized by > 1.3% Al contents (> 2.5% Al_2O_3 contents), while the chemically precipitated cherts (C-cherts) were typically characterized by much lower Al_2O_3 contents (Van den Boorn et al., 2010; Fan et al., 2013; Geilert et al., 2014b; Brengman and Fedo, 2018). Moreover, S-cherts can record a Si-isotope signal identical to that of volcanic rocks, which is close to 0‰ (Georg et al., 2007; Savage et al., 2013; Chemtob et al., 2015), and thus can be easily distinguished from C-cherts. Additionally, the Si-isotope composition of the E–C boundary seawater (> 2.6–2.9‰; Wen et al., 2016) was generally much heavier than that of hydrothermal fluids (~-0.2‰; Van den Boorn et al., 2010). The Si-isotope fractionation in the E–C boundary and Precambrian ocean was mainly under the control of inorganic processes (Ramseyer et al., 2013; Marin-Carbonne et al., 2014), which produced $\triangle^{30}Si_{(solid\text{-}aqueous)}$ values from -2.0‰ to -1.0‰ (Delstanche et al., 2009; Geilert et al., 2014a; Wen et al., 2016). Thus, seawater-derived C-cherts often yield positive $\delta^{30}Si$ values, whereas hydrothermally derived C-cherts are commonly marked by negative $\delta^{30}Si$ values (De La Rocha et al., 2000; Marin-Carbonne et al., 2012; Ramseyer et al., 2013; Geilert et al., 2014b; Li et al., 2014). The $\delta^{30}Si$ values, the Al contents and their relationships (Fig. 6) were broadly applied to distinguish the potential sources of silica in ancient cherts (Van den Boorn et al., 2010; Marin-Carbonne et al., 2012; Ramseyer et al., 2013; Geilert et al., 2014b; Wen et al., 2016). Based on this model, the relatively homogeneous $\delta^{30}Si$ values in the MY and ZY cherts, particularly in the latter, may reflect a single isotopically homogeneous source of silica. However, the broadly changing $\delta^{30}Si$ values in the CYP cherts may have resulted from mixing Si-enriched hydrothermal fluids with seawater or from successive isotopic fractionation (Fig. 6).

The MY cherts were characterized by positive $\delta^{30}Si$ values from 0.5‰ to 0.9‰ (except for one value, -0.3‰) and low Al concentrations (average value of 0.55%), which may reflect major contributions from silica-rich seawater (Fig. 6). For example, Ramseyer et al. (2013) insisted that the ~540-Ma organism-rich laminated cherts from the South Oman Salt Basin (mostly < 1.87% Al_2O_3; $\delta^{30}Si$ = 0.83 ± 0.28‰) were derived from seawater rather than hydrothermal fluids. The ~3.42-Ga black chert bands with mostly positive $\delta^{30}Si$ values (< 0.2% Al_2O_3; $\delta^{30}Si$ = 0.31 ± 0.19‰) from the Barberton Greenstone Belt in South Africa were also preferentially ascribed to seawater contributions (Geilert et al., 2014b). As discussed in Section 5.1.1, the REE of the MY cherts were inherited from precursor carbonates through diagenetic

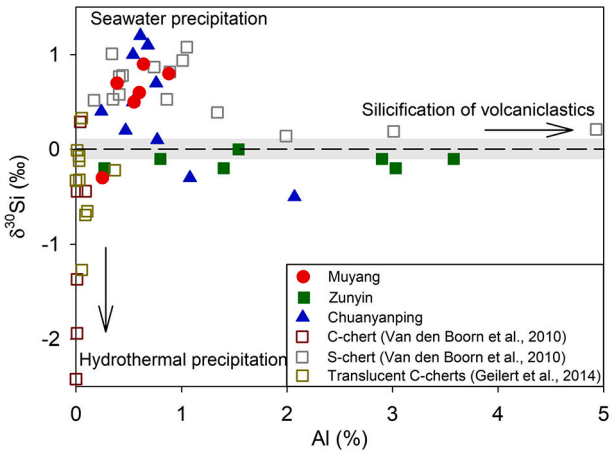

Fig. 6. The relationship between the $\delta^{30}Si$ values and Al contents, through which three origin mechanisms of cherts can be distinguished: 1) seawater-derived cherts with low Al content and positive $\delta^{30}Si$ values, 2) hydrothermally derived cherts with low Al content and negative $\delta^{30}Si$ values, and 3) detritus-derived cherts with a high Al content and near-zero $\delta^{30}Si$ values. S-Chert: silicified chert; C-Chert: chemically precipitated chert (Van den Boorn et al., 2010).

replacement, while the $\delta^{30}Si$ values denoted seawater as the fundamental silica source for the MY cherts. A possible interpretation is that the REE in the precursor carbonates survived diagenetic replacement, while the Si content was limited therein and not sufficient for shaping the cherts; thus, an external Si source from seawater was necessary. Therefore, the silica in these cherts derived from replacing carbonate precursors may have also been derived from Si-enriched seawater.

The ZY cherts were marked by ~0.0‰ $\delta^{30}Si$ values (-0.2‰ to 0.0‰) and high Al concentrations (average value of 1.9%), which suggest volcanic rocks as the primary silica source (Fig. 6; Van den Boorn et al., 2010; Geilert et al., 2014b). The identical $\delta^{30}Si$ values of ~0.0‰ in both the ZY cherts and reported volcanics (Savage et al., 2013; Chemtob et al., 2015) may reflect the complete inheritance of Si isotopes from silicate when these rocks were converted into quartz. Van den Boorn et al. (2010) proposed that the complete inheritance of Si isotopes from silicates may be attributed to incomplete silicification by seawater. For example, in their article (Kitty's Gap stratiform cherts, ~3.5 Ga), partially silicified S-cherts with Al contents from 2.0% to 5.0% had ~0‰ Si-isotope signals, whereas fully silicified cherts with Al contents of < 1.3% yielded Si-isotope signals from ~0.4‰ to ~1.0‰, similar to those of seawater-derived cherts. This observation illustrates that the formation of S-cherts may involve silica from seawater instead of silica that was transformed from silicate. However, the $\delta^{30}Si$ values of the ZY cherts remained almost constant (~0.0‰), although their Al contents (0.27% to 3.58%) covered the range of the Kitty's Gap S-cherts, in which the Si-isotope signals deviated from those in volcanic materials (Van den Boorn et al., 2010). This observation suggests that the ~0‰ $\delta^{30}Si$ values of the ZY cherts were not controlled by the extent of silicification and that the formation of S-cherts may have been predominantly associated with the internal Si cycle. Therefore, we maintain that the ZY cherts may have been formed by the conversion of silicate detritus to quartz through water-rock interactions (Rouchon and Orberger, 2008; Rouchon et al., 2009; Brengman and Fedo, 2018), during which the Si-isotope signals of the silicate may have been predominantly preserved.

The Si-isotope signals of the CYP cherts were previously deciphered by Fan et al. (2013). The low Al contents of < 1.08% (except for one value of 2.07%) suggest that the CYP cherts are mainly C-cherts (Fig. 6). The $\delta^{30}Si$ values of the CYP cherts varied widely (-0.5‰ to 1.2‰) and increased from the bottom to the top of the section (Fig. 7), which may be attributed to gradual mixing with an isotopically heavier Si source or Si-isotope fractionation through successive silica deposition. Negative $\delta^{30}Si$ values (-0.5‰ and -0.3‰) occurred in only the two lowest cherts in this section (CYP-02 and CYP-03) and were similar to the values of modern seafloor hydrothermal fluids (-0.4‰ and -0.2‰; De La Rocha et al., 2000). Hydrothermally derived cherts, such as the Archean translucent cherts from the Barberton Greenstone Belt in South Africa (average $\delta^{30}Si$ value of -0.3‰; Geilert et al., 2014b), are also characterized by negative Si-isotope signals. Therefore, the two lowest CYP cherts with negative $\delta^{30}Si$ values may have originated from hydrothermal fluids. The subsequent transformation towards positive $\delta^{30}Si$ values along the section (Fig. 7) may have resulted from increasing seawater contributions rather than Si-isotope fractionation through successive silica deposition events because the cherts with higher $\delta^{30}Si$ values in the upper section also corresponded to weaker Eu anomalies (Fig. 5B). Moreover, positive $\delta^{30}Si$ values are difficult to obtain in cherts through hydrothermal processes (Marin-Carbonne et al., 2012; Geilert et al., 2014b) because of the significant isotopic fractionation ($\triangle^{30}Si_{(solid\text{-}aqueous)}$ = -2.0‰ to -1.0‰) during silica deposition (Delstanche et al., 2009; Geilert et al., 2014a; Wen et al., 2016). Hydrothermal activity may have stopped between CYP-07 and CYP-08 because the Ba content in the two cherts abruptly and sharply decreased from 5750 ppm to 206 ppm and then remained consistently low (mostly ≤501 ppm; Table 2). Moreover, the $\delta^{30}Si$ values of the five upper CYP cherts (CYP-08 to CYP-11) were comparable to those of the MY cherts (Fig. 6), suggesting that these cherts predominantly originated from chemical precipitation from seawater. Together, the six lower CYP cherts (CYP-02 to CYP-07) had varying degrees of hydrothermal influences, while the five upper cherts (CYP-08 to CYP-11) were mainly derived from seawater.

5.2. Redox conditions recorded by cherts

5.2.1. Indications from rare earth elements

The formation of Ce anomalies in marine sediments predominantly depends on the redox conditions of seawater in association with the oxidation of soluble Ce^{3+} to insoluble Ce^{4+} (German et al., 1991; Bau et al., 1996; Alibo and Nozaki, 1999). In oxic seawater, Ce^{3+} can be easily oxidized to Ce^{4+} by Fe-Mn oxides after strong adsorption onto the latter, which results in extremely negative Ce anomalies in ambient seawater and positive Ce anomalies in Fe-Mn sediments (Bau et al., 1996; Alibo and Nozaki, 1999). In suboxic and anoxic seawater, Ce anomalies are smaller or absent due to the reductive dissolution of Fe-Mn oxide particles (German et al., 1991). The Black Sea, for example, is characterized by stratified redox conditions and shows changing Ce anomalies in the water column. In the oxic surface water (0–76 m), the Ce/Ce* ratio decreases from 0.54 to 0.05 with depth, which results from the adsorption and oxidation scavenging of Ce^{3+} by Mn-oxides (German et al., 1991). In the suboxic zone (76 m–110 m), following the increase in dissolved Mn, the Ce/Ce* ratio shifts systematically from 0.05 to 0.64, which may reflect partial transformation from Ce^{4+} and Mn^{4+} to Ce^{3+} and Mn^{2+}, respectively (German et al., 1991). In the deeper anoxic zone (110–180 m), coupled with the increase in dissolved Fe, the Ce/Ce* ratio increases progressively from 0.6 to 1.0 with depth (German et al., 1991). Below the sulfidic interface at ~180 m, which is characterized by the occurrence of abundant free H_2S, the Ce/Ce* ratio of the seawater remains nearly constant at ~0.9 (German et al., 1991). Therefore, Ce anomalies may be an effective parameter in sediments for evaluating the redox conditions of ambient seawater (Ling et al., 2013; Tostevin et al., 2016).

However, postdepositional diagenesis is likely to modify the Ce/Ce* ratio of sediments, during which the REE patterns are inclined to become progressively enriched in Ce and the Dy/Sm_N ratio decreases (Shields and Stille, 2001). The lack of a relationship between the Ce/Ce* and Dy/Sm_N ratios suggests a negligible alteration of Ce anomalies during diagenetic processes (Fig. 8A). Fig. 8B shows that these samples had real Ce anomalies, rather than those caused by La overabundance

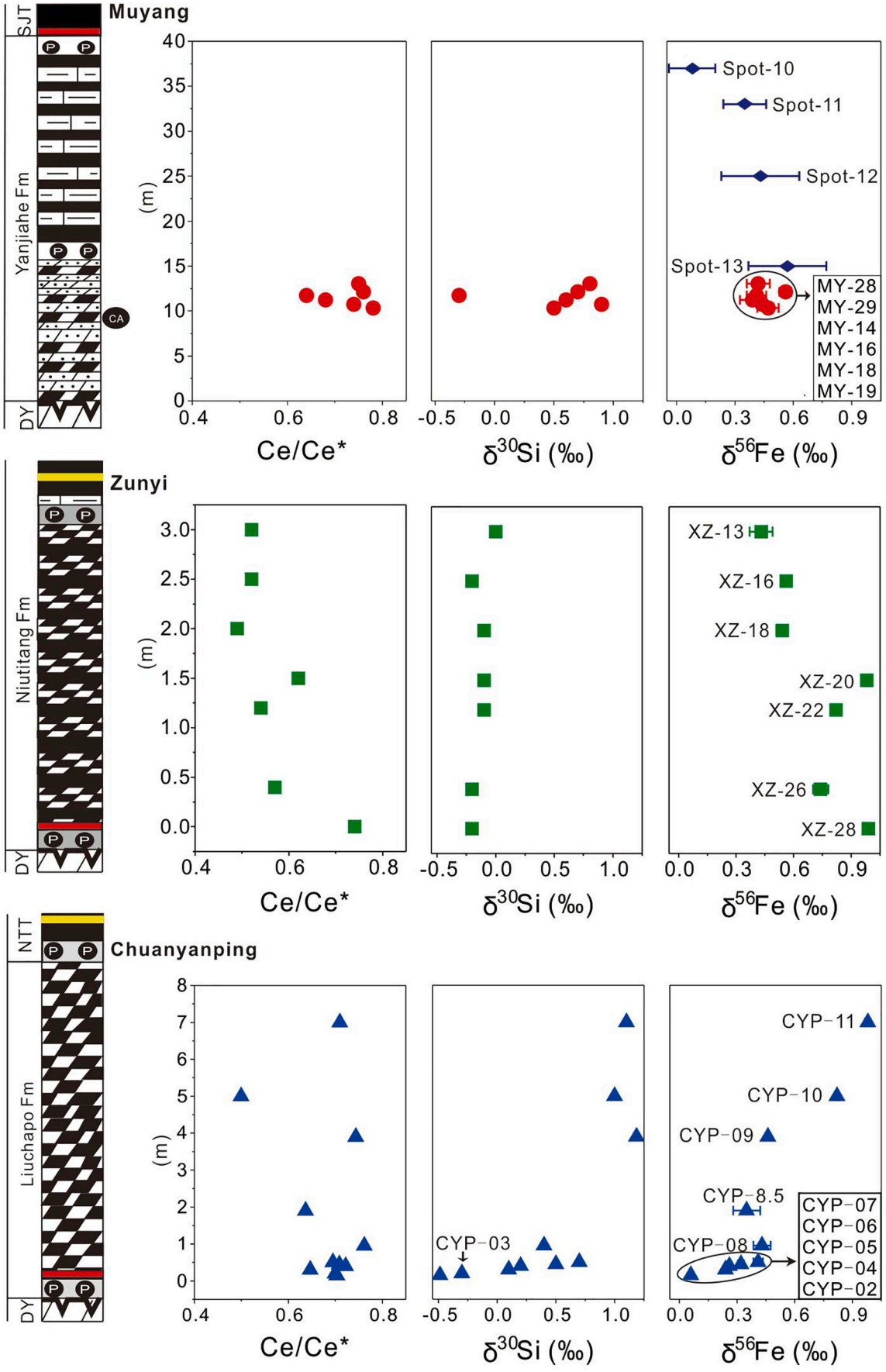

(caption on next page)

Fig. 7. The stratigraphic variations in Ce/Ce* ratios and Si and Fe isotopes in the three studied sections (not showing the abnormal δ^{56}Fe value of -0.41‰ in CYP-03). The data denoted by blue diamond are the average values of in-situ pyrite with five or more data points from Sawaki et al. (2018), who proposed that these pyrites are diagenetic pyrite. The relative positions of these exotic data spots were speculated from Sawaki et al. (2018), in which the total thickness of the Yanjiahe Formation was ~40 m, comparable to our MY section.

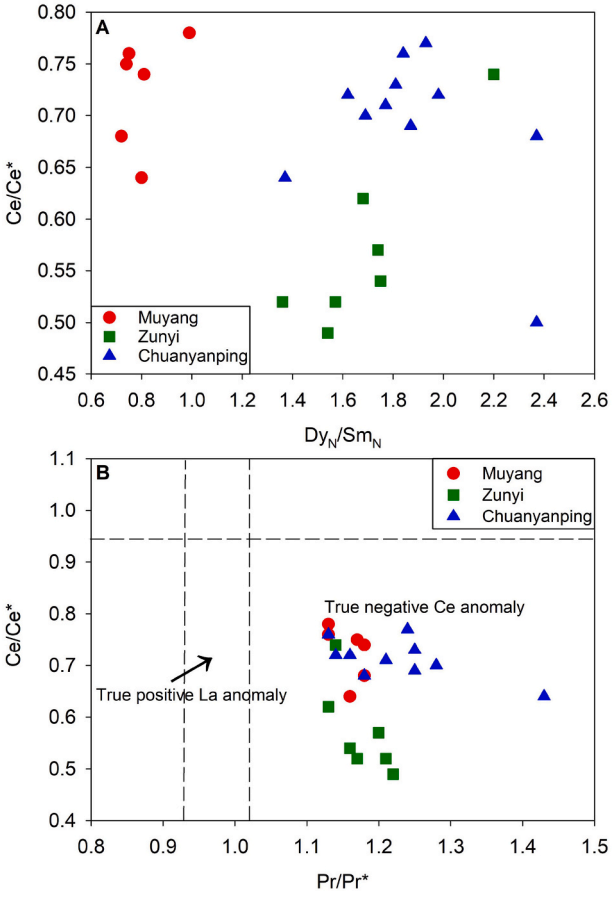

Fig. 8. The Ce/Ce* values plotted against the Dy/Sm$_N$ and Pr/Pr* values. A. The dearth of obvious correlations between Ce/Ce* and Dy/Sm$_N$ ratios reflects the negligible impact of diagenetic alteration on Ce anomalies. B. All cherts show true negative Ce anomalies except one CYP chert with an abnormally high Pr/Pr* value of 2.55 (CYP-10, not presented).

(Ling et al., 2013). The Ce/Ce* ratio in these studied cherts ranged from 0.49 to 0.78, largely overlapping with those of suboxic seawater (0.05 to 0.64) and anoxic seawater (0.6 to 1.0) in the modern stratified ocean (German et al., 1991). Therefore, the Ce anomalies of these cherts suggest a deposition setting near the suboxic/anoxic interface (German et al., 1991), in which the reductive dissolution of Mn and Fe occurred. No obvious changes in the Ce/Ce* ratio occurred in the three studied sections or within a single section, except for slightly lower Ce/Ce* ratios in the ZY section (Fig. 7), which may have resulted from detrital effects (Fig. 3D). Additionally, the Ce/Ce* ratio in modern open ocean is generally less than 0.55 owing to the high oxygen concentration in the modern atmosphere (Alibo and Nozaki, 1999; German et al., 1995; Ling et al., 2013). The shallowest MY cherts yielded a mean Ce/Ce* ratio of 0.72, which may suggest that the overall oxygen level of the ocean and atmosphere at that time was lower than the current value.

The Y/Ho ratio of chondrites is ~27 (Pack et al., 2007), which is often used as a reference for positive or negative Y anomalies in natural samples (Bau et al., 1996). Y and Ho possess identical valences and very similar ionic radii and thus are generally tightly coupled in many geochemical processes, such as magmatic and metamorphic processes (Bolhar et al., 2005; Pack et al., 2007). However, Y and Ho can be substantially fractionated in seawater because of the preferential scavenging of Ho by suspended particles, such as Fe-Mn oxides (Bau et al., 1997; Nozaki et al., 1997). This process may produce a high Y/Ho ratio in seawater, which is typically between 50 and 70 depending on the salinity (Nozaki et al., 1997). However, the Y/Ho ratio decreases from 55 in an oxic water column to 36 under anoxic conditions (Bau et al., 1997). The MY and ZY cherts yielded superchondritic Y/Ho ratios (32 and 39 on average, respectively), which may demonstrate the preferential scavenging of Ho by Fe-Mn oxide particles near a suboxic/anoxic interface, where the reductive dissolution of Mn and Fe occurred (Bau et al., 1997; Nozaki et al., 1997), although contamination of clastic material in the ZY cherts cannot be excluded. Generally, no fractionation occurs between Y and Ho during high-temperature water-rock interactions (Bolhar et al., 2005), resulting in a nearly chondritic Y/Ho ratio of hydrothermal water (~27; Pack et al., 2007). Therefore, the nearly chondritic Y/Ho ratios in the CYP cherts (28 on average) may reflect contributions from submarine hydrothermal fluids. Because of such hydrothermal influences, the Y/Ho ratios do not indicate redox conditions for the formation of the the CYP cherts.

5.2.2. *Indications from iron isotopes*

The Fe-isotope composition of marine sediments is a powerful tool for understanding the Fe redox cycle and seawater redox state (Rouxel et al., 2005; Severmann et al., 2008; Planavsky et al., 2009; Scholz et al., 2014; Sawaki et al., 2018). Although the Fe-isotope composition of marine deposits predominantly depends on the redox state of ambient seawater, detrital materials and early diagenesis may obscure such chemically precipitated signals (Hofmann et al., 2009; Scholz et al., 2014). Continental detritus with a high Al concentration often yields a δ^{56}Fe value of ~0‰ (0 ± 0.05‰; Beard et al., 2003a), whereas chemically deposited sediments with lower Al contents commonly yield a wide range of δ^{56}Fe values depending on the specific redox conditions during their deposition (Rouxel et al., 2005; Severmann et al., 2008; Planavsky et al., 2009). However, no systematic relationship exists between the Fe isotopes and Al contents, which indicates that the Fe-isotope composition of these cherts was not significantly affected by detrital materials (Fig. 9A). During early diagenesis, the primitive Fe oxides in surface sediments may be partially redissolved and released back into seawater through dissimilatory Fe reduction in anoxic environments (Severmann et al., 2008; Scholz et al., 2014a). The partial reductive dissolution of precipitated Fe oxides yields more positive δ^{56}Fe values in the remaining Fe oxides because the released ferrous Fe is isotopically light (Beard et al., 2003a; Balci et al., 2006). If significant diagenetic alteration occurred in these cherts, a clear negative correlation between the δ^{56}Fe values and Fe/Al ratios may be expected, as in the shelf–basin sediments in the Black Sea (Severmann et al., 2008) and the Liuhuiwan cherts reported by Fan et al. (2014). However, there were no pronounced correlations between the δ^{56}Fe values and Fe/Al ratios in any groups of these cherts (Fig. 9B), demonstrating that early diagenesis did not significantly change the Fe-isotope compositions of these cherts. Many studies have also observed that diagenetic processes predominantly involve internal Fe-isotope redistribution and do not significantly change the Fe-isotope composition of bulk sediments (Staubwasser et al., 2006; Severmann et al., 2008; Scholz et al., 2014; Kunzmann et al., 2017). For example, in the northeastern Arabian Sea, the δ^{56}Fe values of reactive Fe(III) increase with depth in the surface sediments (~0–6 cm) due to diagenesis and then remain constant in deeper sediments, whereas the bulk δ^{56}Fe values remain constant throughout the sediments (Staubwasser et al., 2006). Similarly, in the shelf of the Black Sea, the δ^{56}Fe values of pyrite decrease sharply with depth in the surface sediments (~0–5 cm) and then remain constant at

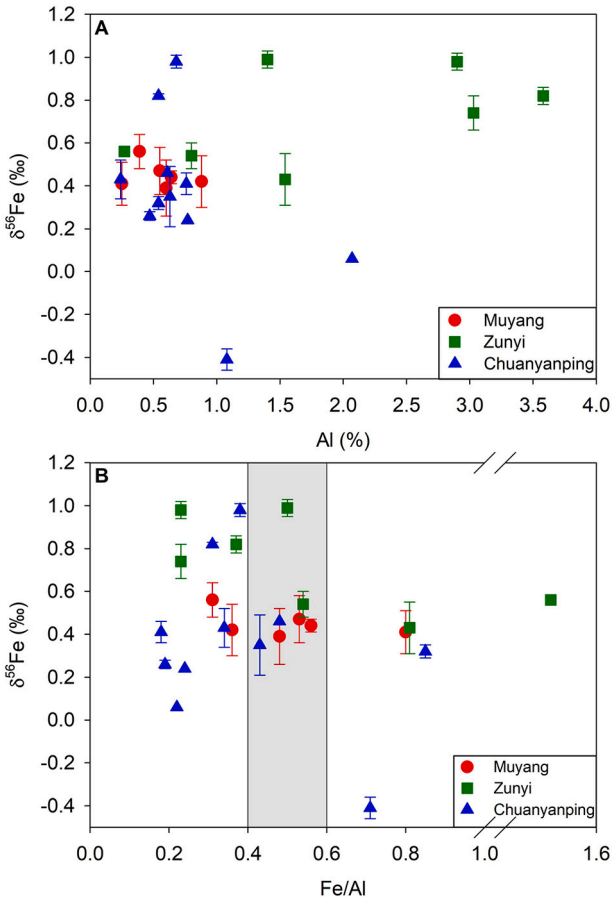

Fig. 9. The δ^{56}Fe values plotted against the Al contents and Fe/Al ratios. A. The absence of an obvious correlation between the δ^{56}Fe values and Al contents suggests negligible detrital contributions to the δ^{56}Fe values. B. No negative correlation between the δ^{56}Fe values and Fe/Al ratios was observed, which implies unimportant alteration of the δ^{56}Fe values during diagenesis. The shaded area reflects the Fe/Al ratio in modern marine sediments (Severmann et al., 2008; Scholz et al., 2014).

greater depths, while the bulk δ^{56}Fe values do not show obvious evolution with depth (Severmann et al., 2008). Severmann et al. (2008) and Scholz et al. (2014) suggested that benthic diagenesis can induce Fe-isotope differences among regions with prominent redox discrepancies but has negligible effects on the local Fe-isotope signals of bulk rocks. Therefore, we argue that most of the studied cherts retained the primary Fe-isotope composition from chemical deposition rather than from detritus or diagenesis.

Generally, the Fe-isotope signals of whole rocks depend on the redox conditions of ambient seawater when detrital and diagenetic influences are excluded. Sediments that are deposited under ferruginous conditions often yield positive δ^{56}Fe values owing to partial Fe oxidation and precipitation (Czaja et al., 2013; Satkoski et al., 2015; Sawaki et al., 2018). In contrast, sediments that precipitate in an oxygenated environment are expected to record ~0‰ δ^{56}Fe values due to complete Fe oxidation and precipitation (Severmann et al., 2008; Planavsky et al., 2009; Fehr et al., 2010). In addition, sediments precipitated in a sulfidic environment are generally characterized by negative δ^{56}Fe values because of pronounced Fe-isotope fractionation from -0.3‰ to -2.8‰ relative to the parent Fe^{2+} solution (Butler et al., 2005; Severmann et al., 2008; Rolison et al., 2018). Therefore, the universally positive δ^{56}Fe values of the studied cherts (mostly 0.06‰ to 0.98‰) may indirectly support a ferruginous setting (Czaja et al., 2013; Satkoski et al., 2015). In the modern ocean, for example, partially ferruginous seawater has been reported near the Rainbow vent and the Loihi seamount, where precipitated Fe^{3+}-bearing oxides display positive δ^{56}Fe values of 0.2–1.2‰ (Severmann et al., 2004; Rouxel et al., 2005; Sawaki et al., 2018). Moreover, positive δ^{56}Fe values of Fe^{3+} oxides in Archean sedimentary rocks are often used as evidence for ferruginous oceans (Planavsky et al., 2012; Czaja et al., 2013). According to Raiswell et al. (2018), the direct identification of ferruginous but not sulfidic conditions is based on Fe-speciation analyses ($Fe_{HR}/Fe_T > 0.38$ and $Fe_{Py}/Fe_{HR} < 0.7$ in sediments). However, Fe-speciation data are suspect if sediments are poor in clastic particles and the total Fe content is < 0.5% (Poulton and Raiswell, 2002; Clarkson et al., 2014; Raiswell et al., 2018). Unfortunately, most of the studied cherts were poor in clastic particles and possessed a total Fe of < 0.5%, so conducting Fe-speciation analysis was not feasible. Nevertheless, previous Fe-speciation data indicated that shelf–slope water masses on the Yangtze Block were dominated by ferruginous conditions across the E–C boundary (Wang et al., 2012b; Wen et al., 2015; Jin et al., 2016; Fan et al., 2018).

Under a ferruginous background, the changeable Fe-isotope compositions of the studied cherts primarily depended on the different oxidation and deposition proportions of dissolved ferrous Fe. Fe isotopic fractionation during abiotic or biotic Fe oxidation mostly follows a Rayleigh model and has often been used to quantify the magnitude of the oxidation scavenging of dissolved ferrous Fe in an assumed closed system (Croal et al., 2004; Planavsky et al., 2009). The δ^{56}Fe value of precipitated Fe oxides was defined as $\delta^{56}Fe_{Fe\text{-}oxide} = \delta^{56}Fe_{initial} + \Delta\ln(f) * f/(1 - f)$, where $\delta^{56}Fe_{initial}$ is the initial isotopic composition of Fe $(II)_{aq}$ in seawater (0.0‰; Johnson et al., 2008), Δ is the isotopic fractionation during the oxidation and precipitation of ferric oxides (1.5‰; Croal et al., 2004), and f is the fraction of $Fe(II)_{aq}$ that remained in solution. Theoretically, the oxidation and deposition proportion of dissolved ferrous Fe (1-f) is close to 100% under a completely oxygenated environment and close to 0% under a strictly anoxic but not sulfidic environment. The Black Sea, for example, is characterized by a redox-stratified water column, in which the level of dissolved Fe^{2+} varies with depth (Lewis and Landing, 1991). The dissolved Fe concentration is low in shallow oxic water at depths of 0–80 m (0.6–4.6 nmol/L) owing to quantitative Fe oxidation and precipitation (Lewis and Landing, 1991). Reductive transformation from Fe^{3+} to Fe^{2+} in deeper water (85–170 m) causes the dissolved Fe concentration to increase systematically with depth (29–297 nmol/L; Lewis and Landing, 1991). The Fe^{3+}/Fe^{2+} chemocline approximately marks the upper limit of a ferruginous zone, according to recent redox classification and calibration by Algeo and Li (2020). The maximum of 296 nmol/L may represent the limit of dissolved Fe in seawater. Based on these data, (1-f) would change from 0% to 90% under ferruginous conditions.

In the MY section (Fig. 7), the studied cherts in the lower Yanjiahe Formation possessed relatively homogeneous δ^{56}Fe values from 0.33‰ to 0.58‰, which corresponded to 81–92% oxidation of ambient ferrous Fe and indicated a consistently ferruginous (less reducing) environment. Notably, the studied MY cherts were deposited slightly earlier than the ZY and CYP cherts, as discussed in Section 2.3. We missed Fe-isotope data for the upper Yanjiahe Formation, which mainly consists of limestones with interbedded black shales and is temporally comparable to the ZY and CYP cherts (Fig. 2). Sawaki et al. (2018) conducted an in-situ Fe-isotope study on diagenetic pyrite in carbonates and black shale across the Yanjiahe Formation at the nearby Sandouping section (several kilometers from MY section). In their study, the δ^{56}Fe values of diagenetic pyrite decreased systematically from ~0.5‰ to ~0‰ (average value of the in-situ data) in the upper Yanjiahe Formation (Fig. 7). Therefore, the upper Yanjiahe Formation may reveal a progressive redox shift from a ferruginous (less reducing) to a completely oxic environment.

In the ZY section, the δ^{56}Fe values of the cherts varied but gradually decreased from the bottom to the top (Fig. 7), which demonstrates that these cherts were deposited under varying redox conditions. The high

δ^{56}Fe values from 0.74‰ to 0.99‰ in the lower cherts, corresponding to 54–72% oxidation of ambient ferrous Fe, reflect ferruginous (more reducing) conditions. In contrast, the low δ^{56}Fe values from 0.44‰ to 0.54‰ in the upper cherts, corresponding to 83–87% oxidation of ambient ferrous Fe, suggest ferruginous (less reducing) conditions. Therefore, there were subtle redox changes from more to less reducing in an overall ferruginous environment from the bottom to the top along the ZY cherts. Such a redox trend towards oxygenation was also recognized in adjacent ZY sections by Zhang et al. (2016) and Li et al. (2018), who found redox transitions from anoxic to oxic or suboxic in the lower Niutitang Formation.

The CYP cherts had variable δ^{56}Fe values that increased upwards along the chert sequences (Fig. 7). The six lower CYP cherts (CYP-02 to CYP-07) may have different degrees of hydrothermal contributions, as discussed in Section 5.1. Hydrothermal activity can also affect the Fe-isotope composition of marine sediments because hydrothermal fluids usually contain high Fe concentrations with negative δ^{56}Fe values (Sharma et al., 2001; Beard et al., 2003b). Indeed, one lower CYP chert (CYP-03) had an extremely negative δ^{56}Fe value of -0.41‰, which may reflect hydrothermal contributions. The oxidation degree of ferrous Fe in the six lower CYP cherts was difficult to quantify because the initial Fe-isotope compositions of hydrothermal fluids vary widely from -0.77‰ to -0.21‰ (Sharma et al., 2001; Beard et al., 2003b). Fortunately, hydrothermal cherts (CYP-02 to CYP-07) occurred only within an ~0.5-m stratigraphic span (the overall sampling span was ~7 m). Interestingly, the five upper CYP cherts, which had an ~6.5-m stratigraphic span, showed large variations in Fe isotopes, with an increasing trend from 0.35‰ to 0.98‰ upwards, reflecting the decreasing oxidation of ambient ferrous Fe from 85–91% to 55–68%. Therefore, an overall ferruginous environment but with a subtle change from less to more reducing may have progressively developed upwards along the CYP cherts (Fig. 10). Such a redox trend towards oxygen depletion was also recognized at a similar slope location by Chen et al. (2019), who found gradual enrichment in reductive species of fixed nitrogen (NH^{4+}) from Cambrian Stage 1 and late Stage 2 to the latest Stage 2.

The Ce/Ce* and Y/Ho ratios demonstrated that these cherts were deposited near a suboxic/anoxic interface, where Mn^{4+} and Fe^{3+} were partially reduced to Mn^{2+} and Fe^{2+}, respectively (German et al., 1991; Lewis and Landing, 1991). Combined with previous studies, ferruginous conditions were indirectly identified by the positive Fe isotopes in these cherts. According to the calibration of redox classification by Algeo and Li (2020), a ferruginous zone may commence at the Fe^{3+}/Fe^{2+} chemocline, but these authors also proposed that ferruginous conditions are equivalent to “suboxic-subreduced” conditions, the upper limit of which is close to the Mn^{4+}/Mn^{2+} chemocline. Therefore, the suboxic-anoxic conditions reflected by the Ce/Ce* and Y/Ho ratios may approximate the ferruginous conditions identified by Fe isotopes. However, the Ce/Ce* and Y/Ho ratios cannot distinguish more subtle discrepancies in overall ferruginous conditions with different levels of dissolved ferrous Fe. A possible explanation is that the Fe-isotope system is more sensitive to redox changes, and redox changes that can be identified by Fe isotopes have not reached the threshold for Ce/Ce* and Y/Ho proxies to respond. This is because the redox potential of Ce^{3+}/Ce^{4+} lies between Fe^{2+}/Fe^{3+} and Mn/Mn^{4+} (Elderfield and Sholkovitz, 1987), and the fractionation of Y/Ho is a side product of the formation and deposition of Fe-Mn oxides (Bau et al., 1997).

5.3. Implications for oceanic chemistry and life evolution

During the early Cambrian, the oceanic redox conditions on the Yangtze Block and their effects on the evolution of life have been extensively investigated (Wang et al., 2012b; Chen et al., 2015; Wen et al., 2015; Li et al., 2017; Xiang et al., 2020). Combined with previously reported Fe-isotope data, the paleo-ocean may have been marked by a stratified redox framework before ~535 Ma in the Cambrian (Fig. 10A). At that time (before ~535 Ma), phosphorites below the ~535-Ma volcanic tuff (Fig. 2) in the MSC section (inner shelf) documented well-oxygenated conditions following their ~0‰ δ^{56}Fe values (Fan et al., 2016). In contrast, the MY cherts (outer shelf) recorded ferruginous (less reducing) conditions, as discussed above. Notably, the lower phosphorites in the MSC section and the lower cherts in the MY section were preliminarily correlated here and may have been deposited approximately but not rigorously simultaneously. Assuming that these two units were deposited simultaneous, stratified redox conditions in the water column may have developed at the Yangtze Block before ~535 Ma in the Cambrian. Additionally, there was a local intra-platform basin near the MY section during the E–C transition (Fig. 1), which may have developed unique water chemistry and potentially affected the MY locale. However, Fan et al. (2018) and Xiang et al. (2020) showed that slope and basin cherts (YJ, SLK, and CY; Fig. 10A) also had ferruginous (less reducing) deposition conditions (~0.3‰ δ^{56}Fe) immediately above the E–C boundary. Therefore, the MY locale may not have been significantly affected by the nearby intra-platform basin. It can be preliminarily concluded that, before ~535 Ma in the Cambrian, the water column on the Yangtze Block was characterized by oxic surface water (MSC), below which the seawater was ferruginous (less reducing) (MY, YJ, SLK, and CY), similar to the stratified redox framework in the early Ediacaran ocean (Li et al., 2010). To date, no more subtle redox changes have been identified by Fe isotopes on the Yangtze Block during this interval.

During ~535–526 Ma, the Fe-isotope trends indicated spatially heterogeneous redox conditions in the water column on the Yangtze Block (Fig. 10B), consistent with the observations in previous studies (Cai et al., 2015; Zhang et al., 2016; Li et al., 2018; Chen et al., 2019). During this period, ~0‰ δ^{56}Fe values in the MSC section (inner shelf) indicated completely oxic seawater conditions with ~100% deposition of dissolved ferrous Fe (Fan et al., 2016). The outer-shelf MY section may have shifted progressively from a ferruginous (less reducing) to a completely oxic environment with the quantitative oxidation of dissolved ferrous Fe (Sawaki et al., 2018). Notably, we cannot exclude the possibility of a local oxygenation signal along the MY section because it was close to an intra-platform basin during the E–C transition (Fig. 1). However, synchronous oxygenation was recorded in the deeper ZY locale as discussed below, indicating that the MY locale may have been connected to open water masses. At the shelf margin, the ZY cherts documented a ferruginous (more reducing) seawater environment, where 54–72% of the dissolved ferrous Fe was oxidized at the early stage. Subsequently, ferruginous (less reducing) conditions may have occurred at the shelf-margin ZY section, as indicated by the ~80–90% oxidation of dissolved ferrous Fe. Previous studies also observed similar oxygenation processes across the lower Niutitang Formation at shelf-margin locations, such as in other nearby ZY sections (Zhang et al., 2016; Li et al., 2018). Interestingly, the slope CYP cherts recorded the opposite trend, changing from less to more reducing conditions in an overall ferruginous environment. A similar redox evolution was also reported in a slope drill core (ZK2012, Chen et al., 2019). In the deeper basin (CY core), the cherts may have experienced steadily ferruginous (less reducing) conditions (~0.3‰ δ^{56}Fe) through Cambrian Stages 1–3 (Xiang et al., 2020).

Based on these spatially heterogeneous redox conditions, the shelf-margin ZY section may have developed a metastable zone of ferruginous (more reducing) conditions sandwiched within ferruginous (less reducing) seawater near ~535 Ma. Although the Fe isotopes in the ZY and CYP sections gradually decreased and increased, respectively, we cannot determine the strict isochronism. Assuming that these changes were simultaneous, a metastable ferruginous (more reducing) zone may have shifted down from the shallower ZY section to the deeper CYP section. In contrast, assuming that these changes were not strictly simultaneous, the varying Fe isotopes may reflect the expansion or contraction of a metastable ferruginous (more reducing) zone in the ZY and CYP sections. Regardless of the isochronism, a metastable ferruginous (more reducing) zone with more reducing conditions may have

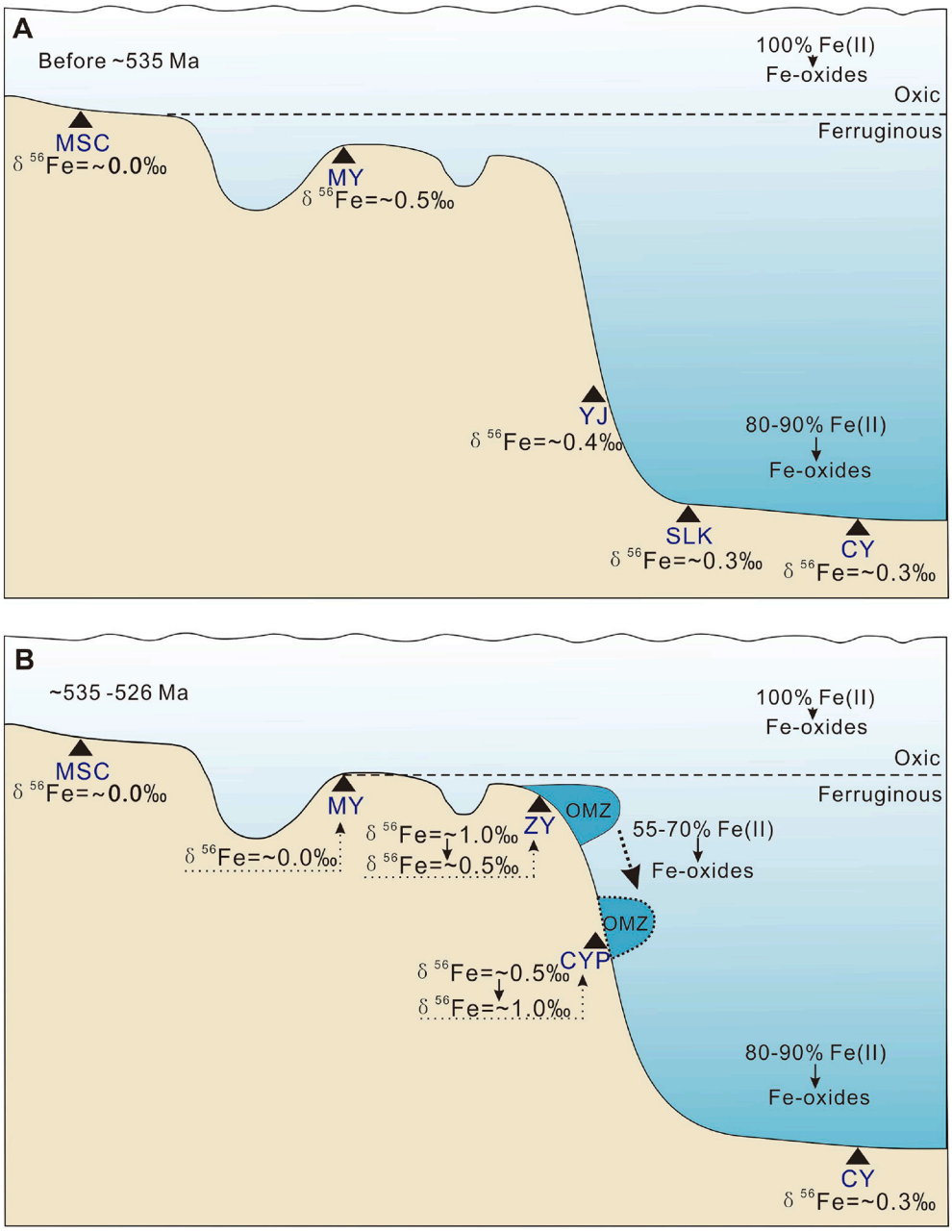

Fig. 10. Conceptual figure of the stratified redox evolution during the early Cambrian (before ~535 Ma and ~535–526 Ma), marked with the approximate sedimentary facies (belts) of our and cited sections in the main text (MSC-Meishucun, MY-Muyang, ZY-Zunyi, CYP-Chuanyanping, YJ-Yinjiang, SLK-Silikou, CY-Chuanye). Before ~535 Ma (A), completely oxic seawater occurred only in the MSC section, below which seawater was mainly ferruginous (less reducing). During ~535–526 Ma (B), oxic seawater gradually extended to the MY section, below which seawater was mainly ferruginous (less reducing), in which a metastable ferruginous (more reducing) zone dynamically occurred at the shelf-slope locations. Data sources: MSC (Fan et al., 2016), MY (here and Sawaki et al., 2018), ZY (here), CYP (here), YJ-Yinjiang (Fan et al., 2018), SLK-Silikou (Fan et al., 2018), CY-Chuanye (Xiang et al., 2020).

dynamically occurred at shelf–slope locations on the Yangtze Block during the early Cambrian (~535–526 Ma), which may have induced the differences in redox conditions along the shelf–slope locations observed in previous studies (Zhang et al., 2016; Cai et al., 2015; Sawaki et al., 2018; Chen et al., 2019). Nevertheless, temporal and spatial comparisons revealed that the water column on the Yangtze Block may have experienced stepwise oxygenation towards the deep water during the early Cambrian (~535–526 Ma; Fig. 10).

The metastable ferruginous (more reducing) zone recognized here may have been a variant of a euxinic wedge in the Precambrian oxygen-depleted ocean or an analogue of the oxygen minimal zone (OMZ) in the modern oxic ocean. In the Precambrian ocean, the development of a metastable zone (euxinic wedge) mainly depended on a lateral gradient of sulfate concentration because the oceanic sulfate concentration at that time was low overall (Li et al., 2010, 2012). However, the formation of an OMZ in the modern sulfate-enriched ocean is primarily associated with locally high marine productivity because subsequent organic-matter decomposition exhausts local oxygen (Thamdrup et al., 2012). Previous studies have shown clear increases in the oxygen and sulfate concentrations and biological expansion in the early Cambrian ocean (Erwin et al., 2011; Cai et al., 2015; Chen et al., 2015), indicating that the controls of forming a metastable redox zone may have transformed gradually across the E–C boundary. For example, Feng et al. (2014) observed that the formation of a metastable redox zone in the water column on the Yangtze Block during Stages 2–3 remained under the control of sulfate-concentration gradients, similarly to the Neoproterozoic ocean (Li et al., 2010). However, Wen et al. (2015) proposed that the metastable redox zone in the water column on the Yangtze Block gradually transformed from a euxinic wedge to an OMZ during the early Cambrian (approximately within Stages 2–3). Recently, Hammarlund et al. (2017) also demonstrated that an OMZ-like environment occurred in the Chengjiang area during Cambrian Stage 3, where and when Chengjiang biota thrived. Moreover, such an OMZ redox framework has been observed worldwide (Baltic Basin) throughout Cambrian Stages 1–5 (Guilbaud et al., 2018). Together, the mechanism of a metastable redox zone during the early Cambrian may

have dynamically changed but gradually evolved towards productivity control as in the modern ocean, although it is likely to revert to a sulfate-control model (Feng et al., 2014). Therefore, our new model, a metastable ferruginous (more reducing) zone nested within ferruginous (less reducing) seawater, is more likely an OMZ analogue that is associated with biological activity (Wen et al., 2015; Hammarlund et al., 2017).

The early Cambrian (~535–526 Ma) is characterized by widespread small shelly fossils, which represent the initial proliferation of animal phyla on Earth (Marshall, 2006; Erwin et al., 2011). At that time, the disappearance of the metastable redox zone in the shallower ZY section and appearance in the deeper CYP section indicate spatial fluctuation of an OMZ-like environment. The OMZ's vertical expansion and oscillation in the modern ocean is mainly associated with fluctuations in oceanic oxygen levels, which are triggered by climate change (Stramma et al., 2008; Moffitt et al., 2014). Additionally, the OMZ's distribution potentially regulates the habitats available to modern oceanic organisms, which in turn affects the OMZ's evolution (Stramma et al., 2011; Bianchi et al., 2013). If the formation of a metastable redox zone depends on biological activity, the spatial shift of the metastable zone observed in this study may have been associated with biological migration. Hammarlund et al. (2017) demonstrated that an OMZ-like environmental barrier during the early Cambrian would have restricted the migration of benthic communities towards the deeper ocean. However, oxygen infiltration and expansion in the ocean would have overcome such a restriction on biological migration towards deeper water. Li et al. (2017), for example, proposed that significant ocean oxygenation during Cambrian Stages 3–4 facilitated biological expansion from shallow-shelf to deep-slope facies on the Yangtze Block. Combined with previous studies, stepwise ocean oxygenation towards deep water was also recognized in the water column on the Yangtze Block during the early Cambrian (~535–526 Ma; Fig. 10). This gradual ocean oxygenation may have precluded the complete oxygenation of the deep ocean on the Yangtze Block during Cambrian Stage 3 or Stage 4, as proposed in previous studies (Wang et al., 2012b; Chen et al., 2015; Xiang et al., 2017). Meanwhile, there was a rapid biological evolution of small shelly fossils from assemblage 1 to assemblage 3, and their spatial distribution expanded from shelf to slope (Jin et al., 2014). Accompanied by oceanic oxygenation, the spatial fluctuation of the OMZ-like metastable zone may have regulated biological distribution and diversification during the early Cambrian (~535–526 Ma). Biological development, in turn, may have contributed to the formation and maintenance of an OMZ-like metastable zone, such as that of the Chengjiang biota (Hammarlund et al., 2017). Therefore, our model provides new insight into redox controls on metazoan diversification in the ocean during the early Cambrian.

6. Conclusions

Three different origins of lower Cambrian cherts on the Yangtze Block were identified in this research. The relatively homogeneous δ^{30}Si values (mostly 0.5‰ to 0.9‰) suggest that the MY cherts were derived from Si-enriched seawater through the alteration of precursor carbonate, reconciling with their seawater-like REE patterns. The ~0‰ δ^{30}Si values indicate the ZY cherts were derived from the replacement of precursor black shales through extensive seawater-rock interactions, during which seawater-like REE patterns were obtained. The six lower CYP cherts with partial negative δ^{30}Si values (up to -0.5‰) and high Ba contents (up to 9950 ppm) originated from hydrothermal fluids to different degrees, whereas the five upper CYP cherts with positive δ^{30}Si values (0.4‰ to 1.1‰) and low Ba contents (mostly ≤501 ppm) originated from Si-enriched seawater. Therefore, most of the cherts preserved seawater chemical signals, except for several lower CYP cherts with hydrothermal contributions. The Ce/Ce* and Y/Ho ratios indicate that these cherts formed under ferruginous conditions overall, while more subtle redox changes were identified by Fe isotopes, namely, ferruginous (less reducing) and ferruginous (more reducing). In combination with a previous study, the Yanjiahe Formation in the MY section (outer shelf) recorded a redox evolution from ferruginous (less reducing) (~0.5‰ δ^{56}Fe) to fully oxygenated (~0‰ δ^{56}Fe) upwards. In the Niutitang Formation in the ZY section (shelf margin), the decreasing δ^{56}Fe values from 0.99‰ to 0.44‰ indicated a redox change from more to less reducing under overall ferruginous conditions over time. The Liuchapo Formation in the CYP section (slope) experienced a redox shift from less to more reducing conditions over time as the δ^{56}Fe values increased from ~0.43‰ to 0.98‰. Temporal and spatial comparisons of our and previously studied sections revealed a stratified redox framework for the early Cambrian ocean. Before ~535 Ma in the Cambrian, the seawater column was primarily characterized by surface oxic conditions and mid-deep ferruginous conditions. During ~535–526 Ma, oxic seawater progressively expanded to the outer shelf (MY section) and a metastable ferruginous (more reducing) zone occurred at the shelf-margin ZY section but subsequently shifted down to the slope CYP section. Therefore, a metastable redox zone may have dynamically occurred at shelf–slope locations on the Yangtze Block during the early Cambrian, which was likely an analogue of the modern OMZ that is associated with biological activity. The occurrence and spatial fluctuation of the metastable redox zone from the shelf-margin ZY to the slope CYP may reflect ocean oxygenation and biological expansion towards deeper water during the early Cambrian (~535–526 Ma). This progressive oxygenation may be a prelude to the oxygenation of the Nanhua Basin during Cambrian Stage 3 or Stage 4, as proposed in previous studies. Therefore, our model provides new insight into redox controls on metazoan diversification in the ocean during the early Cambrian, although more detailed research is still necessary.

Declaration of Competing Interest

Now, we confirm that this manuscript has not been published elsewhere and is not under consideration by another journal. All authors have approved the manuscript and agree with submission to **Palaeogeography Palaeoclimatology Palaeoecology**. The authors have no conflicts of interest to declare.

Acknowledgements

This project was funded by the Strategic Priority Research Program (B) of the Chinese Academy of Sciences (XDB18030302), the National Natural Science Foundation of China (U1812402, 41890840, 41573011, 41873027), CAS IIT (JCTD-2019-17), China geological survey (DD20190002), and the Key Laboratory of Deep-Earth Dynamics of Ministry of Natural Resources (J1901-20-1). We give thanks to two anonymous reviewers for reviewing the manuscript and the editors for providing editorial comments.

Appendix A. Supplementary data

Supplementary data to this article can be found online at https://doi.org/10.1016/j.palaeo.2020.109961.

References

Ahn, S.Y., Zhu, M.Y., 2017. Lowermost Cambrian acritarchs from the Yanjiahe formation, south China: implication for defining the base of the Cambrian in the Yangtze Platform. Geo. Mag. 154 (06), 1–15.

Algeo, T.J., Li, C., 2020. Redox classification and calibration of redox thresholds in sedimentary systems. Geochim. Cosmochim. Acta. https://doi.org/10.1016/j.gca.2020.01.055. (in press).

Alibo, D.S., Nozaki, Y., 1999. Rare earth elements in seawater: particle association, shale-normalization, and Ce oxidation - A study along the slopes of Sagami and Nankai Troughs near Japan. Geochim. Cosmochim. Acta 63 (3–4), 363–372.

André, L., Cardinal, D., Alleman, L.Y., Moorbath, S., 2006. Silicon isotopes in 3.8 Ga West Greenland rocks as clues to the Eoarchaean supracrustal Si cycle. Earth Planet. Sci.

Lett. 245, 162–173.
Balci, N., Bullen, T.D., Witte-Lien, K., Shanks, W.C., Motelica, M., Mandernack, K.W., 2006. Iron isotope fractionation during microbially stimulated Fe(II) oxidation and Fe(III) precipitation. Geochim. Cosmochim. Acta 70, 622–639.
Basu, A.R., Wang, J.W., Huang, W.K., Xie, G.H., Mitsunobu, T., 1991. Major element, REE, and Pb, Nd and Sr isotopic geochemistry of Cenozoic volcanic rocks of eastern China: Implications for their origin from suboceanic-type mantle reservoirs. Earth Planet. Sci. Lett. 105 (1–3), 149–169.
Bau, M., Koschinsky, A., Dulski, P., Hein, J.R., 1996. Comparison of the partitioning behaviours of yttrium, rare earth elements, and titanium between hydrogenetic marine ferromanganese crusts and seawater. Geochim. Cosmochim. Acta 60, 1709–1725.
Bau, M., Moller, P., Dulski, P., 1997. Yttrium and lanthanides in eastern Mediterranean seawater and their fractionation during redox-cycling. Mar. Chem. 56, 123–131.
Beard, B.L., Johnson, C.M., Skulan, J.L., Nealson, K.H., Cox, L., Sun, H., 2003a. Application of Fe isotopes to tracing the geochemical and biological cycling of Fe. Chem. Geol. 195, 87–117.
Beard, B.L., Johnson, C.M., Von Damm, K.L., Poulson, R.L., 2003b. Iron isotope constraints on Fe cycling and mass balance in oxygenated Earth oceans. Geology 31, 629–632.
Bianchi, D., Galbraith, E.D., Carozza, D.A., Mislan, K.A.S., Stock, C.A., 2013. Intensification of open-ocean oxygen depletion by vertically migrating animals. Nat. Geosci. 6 (7), 545–548.
Bolhar, R., Van Kranendonk, M.J., Kamber, B.S., 2005. A trace element study of siderite-jasper banded iron formation in the 3.45 Ga Warrawoona Group, Pilbara Craton-Formation from hydrothermal fluids and shallow seawater. Precambrian Res. 137, 93–114.
Brengman, L.A., Fedo, C.M., 2018. Development of a mixed seawater-hydrothermal fluid geochemical signature during alteration of volcanic rocks in the Archean (~2.7 Ga) Abitibi Greenstone Belt, Canada. Geochim. Cosmochim. Acta 2018, 227–245.
Butler, I.B., Archer, C., Vance, D., Oldroyd, A., Rickard, D., 2005. Fe isotope fractionation on FeS formation in ambient aqueous solution. Earth Planet. Sci. Lett. 236, 430–442.
Cai, C., Xiang, L., Yuan, Y., He, X., Chu, X., Chen, Y., Xu, C., 2015. Marine C, S and N biogeochemical processes in the redox-stratified early Cambrian Yangtze ocean. J. Geol. Soc. 172, 390–406.
Canfield, D.E., Teske, A., 1996. Late Proterozoic rise in atmospheric oxygen concentration inferred from phylogenetic and sulphur-isotope studies. Nature 382, 127–132.
Chang, S., Feng, Q.L., Clausen, S., Zhang, L., 2017. Sponge spicules from the lower Cambrian in the Yanjiahe Formation, South China: The earliest biomineralizing sponge record. Paleogeogr. Paleoclimatol. Paleoecol. 474, 36–44.
Chang, S., Zhang, L., Clausen, S., Bottjer, D.J., Feng, Q., 2019. The Ediacaran-Cambrian rise of siliceous sponges and development of modern oceanic ecosystems. Precambrian Res. 333, 105438.
Chemtob, S.M., Rossman, G.R., Young, E.D., Ziegler, K., Moynier, F., Eiler, J.M., Hurowitz, J.A., 2015. Silicon isotope systematics of acidic weathering of fresh basalts, Kilauea Volcano, Hawai'i. Geochim. Cosmochim. Acta 169, 63–81.
Chen, D.Z., Wang, J.G., Qing, H.R., Yan, D.T., Li, R.W., 2009. Hydrothermal venting activities in the Early Cambrian South China: Petrological, geochronological and stable isotopic constraints. Chem. Geol. 258, 168–181.
Chen, X., Ling, H.F., Vance, D., Shields-Zhou, G.A., Zhu, M.Y., Poulton, S.W., Och, L.M., Jiang, S.Y., Li, D., Cremonese, L., Archer, C., 2015. Rise to modern levels of ocean oxygenation coincided with the Cambrian radiation of animals. Nat. Commun. 6, 7142.
Chen, Y., Diamond, C.W., Stüeken, E.E., Cai, C.F., Gill, B.C., Zhang, F.F., Bates, S.M., Chu, X.L., Ding, Y., Lyons, T.W., 2019. Coupled evolution of nitrogen cycling and redoxcline dynamics on the Yangtze Block across the Ediacaran-Cambrian transition. Geochim. Cosmochim. Acta 257, 243–265.
Clarkson, M.O., Poulton, S.W., Guilbaud, R., Wood, R.A., 2014. Assessing the utility of Fe/Al and Fe-speciation to record water column redox conditions in carbonate-rich sediments. Chem. Geol. 382, 111–122.
Clayton, R.N., Mayeda, T.K., 1963. The use of bromine pentafluoride in the extraction of oxygen from oxides and silicates for isotopic analysis. Geochim. Cosmochim. Acta 27, 43–52.
Croal, L.R., Johnson, C.M., Beard, B.L., Newman, D.K., 2004. Iron isotope fractionation by Fe(II)-oxidizing photoautotrophic bacteria. Geochim. Cosmochim. Acta 68, 1227–1242.
Czaja, A.D., Johnson, C.M., Beard, B.L., Roden, E.E., Li, W., Moorbath, S., 2013. Biological Fe oxidation controlled deposition of banded iron formation in the ca. 3770 Ma Isua Supracrustal Belt (West Greenland). Earth Planet. Sci. Lett. 363, 192–203.
De La Rocha, C.L., Brzezinski, M.A., DeNiro, M.J., 2000. A first look at the distribution of the stable isotopes of silicon in natural waters. Geochim. Cosmochim. Acta 64, 2467–2477.
Delstanche, S., Opfergelt, S., Cardinal, D., Elsass, F., André, L., Delvaux, B., 2009. Silicon isotopic fractionation during adsorption of aqueous monosilicic acid onto iron oxide. Geochim. Cosmochim. Acta 73 (4), 923–934.
Derry, L.A., Jacobsen, S.B., 1990. The chemical evolution of Precambrian seawater-evidence from REEs in banded iron formations. Geochim. Cosmochim. Acta 54, 2965–2977.
Ding, T.P., 2004. Chapter 25-Analytical methods for silicon isotope determinations. In: Handbook of Stable Isotope Analytical Techniques, pp. 523–537.
Dong, L., Xiao, S., Shen, B., Zhou, C., Li, G., Yao, J., 2009. Basal Cambrianmicrofossils from the Yangtze Gorges area (South China) and the Aksu area (TarimBlock, northwestern China). J. Paleontol. 83, 30–44.
Dong, L., Shen, B., Lee, C.T.A., Shu, X.J., Peng, Y., Sun, Y., Tang, Z.H., Rong, H., Lang, X.G., Ma, H.R., Yang, F., Guo, W., 2015. Germanium/silicon of the Ediacaran-Cambrian Laobao cherts: implications for the bedded chert formation and paleoenvironment interpretations. Geochem. Geophys. Geosyst. 16 (3), 751–763.
Dulski, P., 1994. Interferences of oxide, hydroxide and chloride analyte species in the determination of rare-earth elements in geological samples by inductively-coupled plasma-mass spectrometry. Fresen. J. Anal. Chem. 350, 194–203.
Elderfield, H., Sholkovitz, E.R., 1987. Rare earth elements in the pore waters of reducing nearshore sediments. Earth Planet. Sci. Lett. 82 (3), 280–288.
Erwin, D.H., Laflamme, M., Tweedt, S.M., Sperling, E.A., Pisani, D., Peterson, K.J., 2011. The Cambrian conundrum: Early divergence and later ecological success in the early history of animals. Science 334, 1091–1097.
Fan, H.F., Wen, H.J., Hu, R.Z., Zhao, H., 2011. Selenium speciation in Lower Cambrian Se-enriched strata in South China and its geological implications. Geochim. Cosmochim. Acta 75, 7725–7740.
Fan, H.F., Wen, H.J., Zhu, X.K., Hu, R.Z., Tian, S.H., 2013. Hydrothermal activity during Ediacaran-Cambrian transition: Silicon isotopic evidence. Precambrian Res. 224, 23–35.
Fan, H.F., Zhu, X.K., Wen, H.J., Yan, B., Li, J., Feng, L.J., 2014. Oxygenation of Ediacaran Ocean recorded by iron isotopes. Geochim. Cosmochim. Acta 140, 80–94.
Fan, H.F., Wen, H.J., Zhu, X.K., 2016. Marine redox conditions in the early Cambrian ocean: insights from the lower Cambrian phosphorite deposits, south China. J. Earth Sci. 27 (2), 282–296.
Fan, H.F., Wen, H.J., Han, T., Zhu, X.K., Feng, L.J., Chang, H.J., 2018. Oceanic redox condition during the late Ediacaran (551–541 Ma), South China. Geochim. Cosmochim. Acta 238, 343–356.
Fehr, M.A., Andersson, P.S., Hålenius, U., Gustafsson, Ö., Mörth, C.M., 2010. Iron enrichments and Fe isotopic compositions of surface sediments from the Gotland Deep, Baltic Sea. Chem. Geol. 277 (3), 310–322.
Feng, L.J., Li, C., Huang, J., Chang, H.J., Chu, X.L., 2014. A sulfate control on marine mid-depth euxinia on the early Cambrian (ca. 529–521 Ma) Yangtze platform, South China. Precambrian Res. 246, 123–133.
Gao, P., Li, S.J., Lash, G.G., He, Z.L., Xiao, X.M., Zhang, D.W., Hao, Y.Q., 2020. Silicification and Si cycling in a silica-rich ocean during the Ediacaran-Cambrian transition. Chem. Geol. 552 (2020), 119787.
Geilert, S., Vroon, P.Z., Roerdink, D.L., Van Cappellen, P., van Bergen, M.J., 2014a. Silicon isotope fractionation during abiotic silica precipitation at low temperatures: Inferences from flow-through experiments. Geochim. Cosmochim. Acta 142, 95–114.
Geilert, S., Vroon, P.Z., Van Bergen, M.J., 2014b. Silicon isotopes and trace elements in chert record early Archean basin evolution. Chem. Geol. 386, 133–142.
Georg, R.B., Reynolds, B.C., West, A.J., Burton, K.W., Halliday, A.N., 2007. Silicon isotope variations accompanying basalt weathering Iceland. Earth Planet. Sci. Lett. 261, 476–490.
German, C.R., Holliday, B.P., Elderfield, H., 1991. Redox cycling of rare earth elements in the suboxic zone of the Black Sea. Geochim. Cosmochim. Acta 55, 3553–3558.
German, C.R., Masuzawa, T., Greaves, M.J., Elderfield, H., Edmond, J.M., 1995. Dissolved rare-earth elements in the Southern-Ocean - cerium oxidation and the influence of hydrography. Geochim. Cosmochim. Acta 59, 1551–1558.
Goldberg, T., Strauss, H., Guo, Q.J., Liu, C.Q., 2007. Reconstructing marine redox conditions for the Early Cambrian Yangtze Platform: Evidence from biogenic sulphur and organic carbon isotopes. Paleogeogr. Paleoclimatol. Paleoecol. 254, 175–193.
Graham, J.B., Dudley, R., Aguilar, N.M., Gans, C., 1995. Implications of the late Palaeozoic oxygen pulse for physiology and evolution. Nature 375, 117–120.
Guilbaud, R., Slater, B.J., Poulton, S.W., Harvey, T.H.P., Brocks, J.J., Nettersheim, B.J., Butterfield, N.J., 2018. 2018. Oxygen minimum zones in the early Cambrian ocean. Geochem. Perspect. Lett. 6, 33–38.
Guo, J.F., Li, Y., Li, G.X., 2014. Small shelly fossils from the early Cambrian Yanjiahe Formation, Yichang, Hubei, China. Gondwana Res. 25 (3), 999–1007.
Hammarlund, E.U., Gaines, R.R., Prokopenko, M.G., Qi, C., Hou, X.G., Canfield, D.E., 2017. Early Cambrian oxygen minimum zone-like conditions at Chengjiang. Earth Planet. Sci. Lett. 475, 160–168.
Heck, P.R., Huberty, J.M., Kita, N.T., Ushikubo, T., Kozdon, R., Valley, J.W., 2011. SIMS analyses of silicon and oxygen isotope ratios for quartz from Archean and Paleoproterozoic banded iron formations. Geochim. Cosmochim. Acta 75, 5879–5891.
Hofmann, A., Bekker, A., Rouxel, O., Rumble, D., Master, S., 2009. Multiple sulphur and iron isotope composition of detrital pyrite in Archaean sedimentary rocks: A new tool for provenance analysis. Earth Planet. Sci. Lett. 286, 436–445.
Huang, J., Liu, J., Zhang, Y.N., Chang, H.L., Huang, F., Qin, L.P., 2018. Cr isotopic composition of the Laobao cherts during the Ediacaran–Cambrian transition in south China. Chem. Geol. 482, 121–130.
Jiang, G.Q., Kennedy, M.J., Christie-Blick, N., 2003. Stable isotopic evidence for methane seeps in Neoproterozoic postglacial cap carbonates. Nature 426, 822–826.
Jiang, S.Y., Pi, D.H., Heubeck, C., Frimmel, H., Liu, Y.P., Deng, H.L., Ling, H.F., Yang, J.H., 2009. Early Cambrian ocean anoxia in South China. Nature 459, E5–E6.
Jiang, G.Q., Wang, X.Q., Shi, X.Y., Xiao, S.H., Zhang, S.H., Dong, J., 2012. The origin of decoupled carbonate and organic carbon isotope signatures in the early Cambrian (ca. 542–520 Ma) Yangtze platform. Earth Planet. Sci. Lett. 317-318, 96–110.
Jin, C.S., Li, C., Peng, X.F., Cui, H., Shi, W., Zhang, Z.H., Luo, G.M., Xie, S.C., 2014. Spatiotemporal variability of ocean chemistry in the early Cambrian, South China. Sci. China Earth Sci. 57 (4), 579–591.
Jin, C.S., Li, C., Algeo, T.J., Planavsky, N.J., Cui, H., Yang, X.L., Zhao, Y.L., Zhang, X.L., Xie, S.C., 2016. A highly redox-heterogeneous ocean in South China during the early Cambrian (~529-514 Ma): Implications for biota-environment coevolution. Earth Planet. Sci. Lett. 441, 38–51.
Johnson, C.M., Beard, B.L., Klein, C., Beukes, N.J., Roden, E.E., 2008. Iron isotopes constrain biologic and abiologic processes in banded iron formation genesis. Geochim. Cosmochim. Acta 72 (1), 151–169.
Kimura, H., Watanabe, Y., 2001. Oceanic anoxia at the precambrian-cambrian boundary.

Geology 29 (11), 995.
Knoll, A.H., Caroll, S.B., 1999. Early animal evolution: Emerging views from comparative biology and geology. Science 284, 2129–2137.
Kunzmann, M., Gibson, T.M., Halverson, G.P., Hodgskiss, M.S.W., Bui, T.H., Carozza, D.A., 2017. Iron isotope biogeochemistry of Neoproterozoic marine shales. Geochim. Cosmochim. Acta 209, 85–105.
Lewis, B.L., Landing, W.M., 1991. The biogeochemistry of manganese and iron in the Black Sea. Deep-Sea Res. 38, S773–S803.
Li, Z.-X., Bogdanova, S., Collins, A., Davidson, A., De Waele, B., Ernst, R., Fitzsimons, I., Fuck, R., Gladkochub, D., Jacobs, J., 2008. Assembly, configuration, and break-up history of Rodinia: A synthesis. Precambrian Res. 160, 179–210.
Li, C., Love, G.D., Lyons, T.W., Fike, D.A., Sessions, A.L., Chu, X.L., 2010. A stratified redox model for the Ediacaran ocean. Science 328, 80–83.
Li, C., Love, G.D., Lyons, T.W., Scott, C.T., Feng, L.J., Huang, J., Chang, H.J., Zhang, Q.R., Chu, X.L., 2012. Evidence for a redox stratified Cryogenian marine basin, Datangpo Formation, South China. Earth Planet Sci Lett. 331-332, 246–256.
Li, Y.H., Hou, K.J., Wan, D.F., Zhang, Z.J., Yue, G.L., 2014. Precambrian banded iron formations in the North China Craton: Silicon and oxygen isotopes and genetic implications. Ore Geol. Rev. 57, 299–307.
Li, C., Jin, C.S., Planavsky, N.J., Algeo, T.J., Cheng, M., Yang, X.L., Zhao, Y.L., Xie, S.C., 2017. Coupled oceanic oxygenation and metazoan diversification during the early–middle Cambrian? Geology 45, 743–746.
Li, J., Tang, S., Zhang, S., Xi, Z., Yang, N., Yang, G., Li, L., Li, Y., 2018. Paleo-environmental conditions of the Early Cambrian Niutitang Formation in the Fenggang area, the southwestern margin of the Yangtze Platform, southern China: Evidence from major elements, trace elements and other proxies. J. Asian Earth Sci. 159, 81–97.
Ling, H.F., Chen, X., Li, D., Wang, D., Shields-Zhou, G.A., Zhu, M.Y., 2013. Cerium anomaly variations in Ediacaran-earliest Cambrian carbonates from the Yangtze Gorges area, South China: Implications for oxygenation of coeval shallow seawater. Precambrian Res. 225, 110–127.
Marin-Carbonne, J., Chaussidon, M., Robert, F., 2012. Micrometer-scale chemical and isotopic criteria (O and Si) on the origin and history of Precambrian cherts: Implications for paleo-temperature reconstructions. Geochim. Cosmochim. Acta 92, 129–147.
Marin-Carbonne, J., Robert, F., Chaussidon, M., 2014. The silicon and oxygen isotope compositions of Precambrian cherts: A record of oceanic paleo-temperatures? Precambrian Res 247, 223–234.
Marshall, C.R., 2006. Explaining the Cambrian “explosion” of animals. Annu. Rev. Earth Planet. Sci. Lett. 34, 355–384.
Moffitt, S.E., Hill, T.M., Ohkushi, K., Kennett, J.P., Behl, R.J., 2014. Vertical oxygen minimum zone oscillations since 20 ka in Santa barbara basin: A benthic foraminiferal community perspective. Paleoceanography 29 (1), 44–57.
Nothdurft, L.D., Webb, G.E., Kamber, B.S., 2004. Rare earth element geochemistry of Late Devonian reefal carbonates, Canning Basin, Western Australia: Confirmation of a seawater REE proxy in ancient limestones. Geochim. Cosmochim. Acta 68 (2), 263–283.
Nozaki, Y., Zhang, J., Amakawa, H., 1997. The fractionation between Y and Ho in the marine environment. Earth Planet. Sci. Lett. 148, 329–340.
Okada, Y., Sawaki, Y., Komiya, T., Hirata, T., Takahata, N., Sano, Y., Han, J., Maruyama, S., 2014. New chronological constraints for Cryogenian to Cambrian rocks in the Three Gorges, Weng'an and Chengjiang areas, South China. Gondwana Res. 25, 1027–1044.
Pack, A., Russell, S.S., Shelley, J.M.G., Van Zuilen, M., 2007. Geo- and cosmochemistry of the twin elements yttrium and holmium. Geochim. Cosmochim. Acta 71, 4592–4608.
Pages, A., Barnes, S., Schmid, S., Coveney Jr., R.M., Schwark, L., Liu, W., Grice, K., Fan, H.F., Wen, H.J., 2018. Geochemical investigation of the lower Cambrian mineralised black shales of South China and the late Devonian Nick deposit, Canada. Ore Geol. Rev. 94, 396–413.
Planavsky, N., Rouxel, O., Bekker, A., Hofmann, A., Little, C.T.S., Lyons, T.W., 2012. Iron isotope composition of some Archean and Proterozoic iron formations. Geochim. Cosmochim. Acta 80, 158–169.
Planavsky, N., Rouxel, O., Bekker, A., Shapiro, R., Fralick, P., Knudsen, A., 2009. Iron-oxidizing microbial ecosystems thrived in late Paleoproterozoic redox-stratified oceans. Earth Planet. Sci. Lett. 286 (1-2), 230–242.
Poulton, S.W., Raiswell, R., 2002. The low-temperature geochemical cycle of iron: from continental fluxes to marine sediment deposition. Am. J. Sci. 302, 774–805.
Qi, L., Hu, J., Gregoire, D.C., 2000. Determination of trace elements in granites by inductively coupled plasma mass spectrometry. Talanta 51, 507–513.
Raiswell, R., Hardisty, D.S., Lyons, T.W., Canfield, D.E., Owens, J.D., Planavsky, N.J., Poulton, S.W., Reinhard, C.T., 2018. The iron paleoredox proxies: A guide to the pitfalls, problems and proper practice. Am. J. Sci. 318 (5), 491–526.
Ramseyer, K., Amthor, J.E., Matter, A., Pettke, T., Wille, M., Fallick, A.E., 2013. Primary silica precipitate at the Precambrian/Cambrian boundary in the South Oman Salt Basin, Sultanate of Oman. Mar. Pet. Geol. 39 (1), 187–197.
Rolison, J.M., Stirling, C.H., Middag, R., Gault-Ringold, M., George, E., Rijkenberg, M.J.A., 2018. Iron isotope fractionation during pyrite formation in a sulfidic Precambrian ocean analogue. Earth Planet. Sci. Lett. 488, 1–13.
Rouchon, V., Orberger, B., 2008. Origin and mechanisms of K–Si-metasomatism of ca.3.4-3.3 Ga volcaniclastic deposits and implications for Archean seawater evolution: Examples from cherts of Kittys Gap (Pilbara craton, Australia) and Msauli (Barberton Greenstone Belt, South Africa). Precambrian Res. 165 (3–4), 169–189.
Rouchon, V., Orberger, B., Hofmann, A., Pinti, D.L., 2009. Diagenetic Fe-carbonates in Paleoarchean felsic sedimentary rocks (Hooggenoeg Formation, Barberton greenstone belt, South Africa): Implications for CO_2 sequestration and the chemical budget of seawater. Precambrian Res. 172 (3–4), 255–278.
Rouxel, O.J., Bekker, A., Edwards, K.J., 2005. Iron isotope constraints on the Archean and Paleoproterozoic ocean redox state. Science (80-) 307 (5712), 1088–1091.
Satkoski, A.M., Beukes, N.J., Li, W., Beard, B.L., Johnson, C.M., 2015. A redox-stratified ocean 3.2 billion years ago. Earth Planet. Sci. Lett. 430, 43–53.
Savage, P.S., Georg, R.B., Williams, H.M., Halliday, A.N., 2013. The silicon isotope composition of the upper continental crust. Geochim. Cosmochim. Acta 109, 384–399.
Sawaki, Y., Tahata, M., Komiya, T., Hirata, T., Han, J., Shu, D.G., 2018. Redox history of the three gorges region during the Ediacaran and early Cambrian as indicated by the Fe isotope. Geosci. Front. 9, 155–172.
Scholz, F., Severmann, S., McManus, J., Hensen, C., 2014. Beyond the Black Sea paradigm: The sedimentary fingerprint of an open-marine iron shuttle. Geochim. Cosmochim. Acta 127, 368–380.
Severmann, S., Johnson, C.M., Beard, B.L., German, C.R., Edmonds, H.N., Chiba, H., Green, D.R.H., 2004. The effect of plume processes on the Fe isotope composition of hydrothermally derived Fe in the deep ocean as inferred from the Rainbow vent site, Mid-Atlantic Ridge, 36°14′N. Earth Planet. Sci. Lett. 225, 63–76.
Severmann, S., Lyons, T.W., Anbar, A., McManus, J., Gordon, G., 2008. Modern iron isotope perspective on the benthic iron shuttle and the redox evolution of ancient oceans. Geology 36, 487–490.
Sharma, M., Polizzotto, M., Anbar, A.D., 2001. Iron isotopes in hot springs along the Juande Fuca Ridge. Earth Planet. Sci. 194, 39–51.
Shen, B., Ma, H., Ye, H., Lang, X.G., Peic, H.X., Zhou, C.M., Zhang, S.H., Yang, R.Y., 2018. Hydrothermal origin of syndepositional chert bands and nodules in the Mesoproterozoic Wumishan Formation: Implications for the evolution of Mesoproterozoic cratonic basin, North China. Precambrian Res. 310, 213–228.
Shields, G., Stille, P., 2001. Diagenetic constraints on the use of cerium anomalies as palaeoseawater redox proxies: An isotopic and REE study of Cambrian phosphorites. Chem. l Geol. 175, 29–48.
Sperling, E.A., Wolock, C.J., Morgan, A.S., Gill, B.C., Kunzmann, M., Halverson, G.P., Macdonald, F.A., Knoll, A.H., Johnston, D.T., 2015. Statistical analysis of iron geochemical data suggests limited late Proterozoic oxygenation. Nature 523, 451–454.
Staubwasser, M., von Blanckenburg, F., Schoenberg, R., 2006. Iron isotopes in the early marine diagenetic iron cycle. Geology 34 (8), 629–632.
Steiner, M., Wallis, E., Erdtmann, B.-D., Zhao, Y.L., Yang, R.D., 2001. Submarine hydrothermal exhalative ore layers in black shales from South China and associated fossils—insights into a Lower Cambrian facies and bio-evolution. Paleogeogr. Paleoclimatol. Paleoecol. 169, 165–191.
Stramma, L., Johnson, G.C., Sprintall, J., Mohrholz, V., 2008. Expanding oxygen-minimum zones in the tropical oceans. Science 320 (5876), 655–658.
Stramma, L., Prince, E.D., Schmidtko, S., Luo, J., Hoolihan, J.P., Visbeck, M., Wallace, D.W.R., Brandt, P., Körtzinger, A., 2011. Expansion of oxygen minimum zones may reduce available habitat for tropical pelagic fishes. Nat. Clim. Change 2 (1), 33–37.
Stuben, D., Taibi, N.E., McMurtry, G.M., Scholten, J., Stoffers, P., Zhang, D., 1994. Growth history of a hydrothermal silica chimney from the Marian back-arc spreading center (southwest Pacific, 18o13'N). Chem. Geol. 113, 273–296.
Tang, S.H., Zhu, X.K., Cai, J.J., Li, S.Z., He, X.X., Wang, J.H., 2006. Chromatographic separation of Cu, Fe and Zn using AGMP-1 anion exchange resin for isotope determination by MC-ICPMS. Rock Miner. Anal. 25, 11–14.
Tatzel, M., von Blanckenburg, F., Oelze, M., Schuessler, J.A., Bohrmann, G., 2015. The silicon isotope record of early silica diagenesis. Earth Planet. Sci. Lett. 428, 293–303.
Thamdrup, B., Dalsgaard, T., Revsbech, N.P., 2012. Widespread functional anoxia in the oxygen minimum zone of the eastern South Pacific. Deep-Sea Res Part I. 65, 36–45.
Tostevin, R., Shields, G.A., Tarbuck, G.M., He, T., Wood, R.A., 2016. Effective use of cerium anomalies as a redox proxy in carbonate-dominated marine settings. Chem. Geol. 438, 146–162.
Urabe, T., Kusakabe, M., 1990. Barite silica chimneys from the Sumisu Rift, Izu-Bonin Arc: Possible analog to hematitic chert associated with Kuroko deposits. Earth Planet. Sci. Lett. 100, 283–290.
Van den Boorn, S.H.J.M., van Bergen, M.J., Vroon, P.Z., de Vries, S.T., Nijman, W., 2010. Silicon isotope and trace element constraints on the origin of 3.5 Ga cherts: Implications for Early Archaean marine environments. Geochim. Cosmochim. Acta 74 (3), 1077–1103.
Wang, J., Li, Z.X., 2003. History of Neoproterozoic rift basins in South China: Implications for Rodinia break-up. Precambrian Res. 122, 141–158.
Wang, J.G., Chen, D.Z., Wang, D., Yan, D.T., Zhou, X.Q., Wang, Q.C., 2012a. Petrology and geochemistry of chert on the marginal zone of Yangtze Platform, western Hunan, South China, during the Ediacaran–Cambrian transition. Sedimentology 59, 809–829.
Wang, J.G., Chen, D.Z., Yan, D.T., Wei, H.Y., Xiang, L., 2012b. Evolution from an anoxic to oxic deep ocean during the Ediacaran-Cambrian transition and implications for bioradiation. Chem. Geol. 306-307, 129–138.
Wei, G.Y., Planavsky, N.J., Tarhan, L.G., Chen, X., Ling, H.F., 2018. Erratum: marine redox fluctuation as a potential trigger for the cambrian explosion. Geology 46 (8).
Wen, H.J., Fan, H.F., Zhang, Y.X., Cloquet, C., Carignan, J., 2015. Reconstruction of early Cambrian ocean chemistry from Mo isotopes. Geochim. Cosmochim. Acta 164, 1–16.
Wen, H.J., Fan, H.F., Tian, S.H., Wang, Q.L., Hu, R.Z., 2016. The formation conditions of the early Ediacaran cherts, south China. Chem. Geol. 430, 45–69.
Xiang, L., Schoepfer, S.D., Shen, S.Z., Cao, C.Q., Zhang, H., 2017. Evolution of oceanic molybdenum and uranium reservoir size around the Ediacaran–Cambrian transition: Evidence from western Zhejiang, south China. Earth Planet. Sci. Lett. 464, 84–94.
Xiang, L., Schoepfer, S.D., Zhang, H., Chen, Z.W., Cao, C.Q., Shen, S.Z., 2020. Deep-water dissolved iron cycling and reservoir size across the Ediacaran-Cambrian transition. Chem. Geol. 541, 119575.
Xu, L.G., Lehmann, B., Mao, J., Qu, W., Du, A., 2011. Re-Os age of polymetallic Ni-Mo-PGE-Au mineralization in Early Cambrian Black Shales of South China-A reassessment. Econ. Geol. 106, 511–522.
Yang, B., Steiner, M., Zhu, M.Y., Li, G.X., Liu, J.N., Liu, P.J., 2016. Transitional

Ediacaran–Cambrian small skeletal fossil assemblages from South China and Kazakhstan: Implications for chronostratigraphy and metazoan evolution. Precambrian Res. 285, 202–215.
Zhang, J.P., Fan, T.L., Algeo, T.J., Li, Y.F., Zhang, J.C., 2016. Paleo-marine environments of the Early Cambrian Yangtze Platform. Palaeogeogr. Palaeoclimatol. Palaeoecol. 443, 66–79.
Zhao, X.M., Zhang, H.F., Zhu, X.K., Tang, S.H., Yan, B., 2012. Iron isotope evidence for multistage melt–peridotite interactions in the lithospheric mantle of eastern China. Chem. Geol. 292-293, 127–139.
Zhong, S., Mucci, A., 1995. Partitioning of rare earth elements (REEs) between calcite and seawater solutions at 25 °C and 1 atm, and high dissolved REE concentrations. Geochim. Cosmochim. Acta 59 (3), 443–453.
Zhu, M.Y., Zhang, J.M., Steiner, M., Yang, A.H., Li, G.X., Erdtman, B.D., 2003. Sinian-Cambrian stratigraphic framework for shallow- to deep-water environments of the Yangtze Platform: An integrated approach. Prog. Nat. Sci. 13, 951–960.
Zhu, R.X., Li, X.H., Hou, X.G., Pan, Y.X., Wang, F., Deng, C.L., He, H.Y., 2009. SIMSU–Pb zircon age of a tuff layer in the Meishucun section, Yunnan, southwest China: Constraint on the age of the Precambrian–Cambrian boundary. Sci. China Ser. D: Earth Sci. 52, 1385–1392.
Ziegler, K., Marin-Carbonne, J.M., 2012. Silicon and oxygen isotopes during diagenesis of the Monterey chert. In: Goldschmidt Conference Abstracts, pp. 2603.